Journal of Fluids and Structures 119 (2023) 103892

Contents lists available at ScienceDirect

Journal of Fluids and Structures

journal homepage: www.elsevier.com/locate/jfs

Experimental and numerical investigation of an aircraft wing with hinged wingtip for gust load alleviation

Davide Balatti [a,*,1], Hamed Haddad Khodaparast [a], Michael I. Friswell [a], Marinos Manolesos [b], Andrea Castrichini [c]

[a] Swansea University, Faculty of Science and Engineering, Bay Campus, Swansea, SA1 8EN, United Kingdom
[b] City, University of London, Northampton Square, London EC1V 0HB, United Kingdom
[c] Airbus Operations Ltd, Bristol, BS34 7QQ, United Kingdom

ARTICLE INFO

Article history:
Received 21 October 2022
Received in revised form 8 February 2023
Accepted 8 April 2023
Available online xxxx

Keywords:
Gust load alleviation
Wind tunnel testing
Hinged wingtips
Model validation

ABSTRACT

A recent consideration in aircraft design is using hinged wing tip devices to increase the aspect ratio, improving aircraft performance. Moreover, numerical studies have suggested using the wingtips during flight to provide additional gust load alleviation ability. This work aims to experimentally validate aeroelastic models of a wing with fixed and hinged wingtips. Validated numerical models of wings with hinged wingtips are essential to improve predictions and system knowledge and as a reference model for design optimisation. An elastic wing with hinged and fixed wingtips with different weights was tested. Static wind tunnel tests confirmed the ability of hinged wingtips to reduce gust loads. Aeroelastic models of the wing with the manufactured wingtips were developed, and time history gust responses validated the models. The validated models drove the design of a more efficient wingtip, which experimentally proved the improvement of load alleviation by reducing its mass and structural inertia. Based on this, a parametric study highlighted that increasing the wingtip mass alone, reducing the spanwise distance of the wingtip centre of mass from the hinge, or reducing the hinge stiffness reduces the maximum wing root bending moment.

1. Introduction

Performance optimisation is a fundamental aspect of aircraft design. Nowadays, huge efforts have been made to find techniques that reduce aerodynamic drag. A considerable contribution, usually 30%–40% of the overall drag, is lift induced drag, which could be reduced by increasing the aspect ratio. However, such a design solution has some limitations related to the maximum aircraft dimensions allowed at airports and also to the increase in bending moments along the wing. A possible solution to the first problem is to use a folding wing that can be deployed on the ground. An example of this technique is the latest version of the Boeing B777X, which, through the use of wingtips, the wingspan is 7 metres longer than that of the original B777. The folding wingtip capability will be used only on the ground during taxi to and from the gates allowing the aircraft to fit within the airport gate. The concept of folding wingtips has been used on several aircraft (Barbarino et al., 2011). Over the years, hinged wings have been used for gust load alleviation (Anon, 1951), for

* Corresponding author.
E-mail address: davide.balatti@swansea.ac.uk (D. Balatti).
[1] Research assistant.

https://doi.org/10.1016/j.jfluidstructs.2023.103892

maximising the wingspan of the aircraft during cruise operation while reducing wing bending moment during extreme flight manoeuvrers (Allen, 1999) and for aeroelastic tailoring (Pitt, 2004).

Recently, Pattinson et al. (2015) showed the potential of a folding wingtip to alleviate the wing loads by coupling a flexible multi-body dynamics solver with a computational fluid dynamics coupled with the structural model. Wilson et al. (2017) defined the flare angle as the angle between the longitudinal axis of the aircraft and the hinge rotation axis and showed that for short-range aircraft, a zero stiffness flared hinge reduces gust and manoeuvre loads. The use of a zero stiffness hinge could cause flutter which can be stabilised via tip masses, the choice of hinge location and hinge flare angle. The choice of hinge flare and hinge location has a small effect on the bending moment at the wing root. Similarly Castrichini et al. (2017b) investigated the effects of using a folding wingtip as a load alleviation device considering a numerical aeroelastic model of a typical commercial jet aircraft. In this work, they investigated the effect of hinge stiffness, damping, hinge orientation and wingtip mass on the static loads, gusts loads and flutter behaviour. For low hinge spring stiffness and wingtip mass, an increase in the hinge angle with respect to the free stream direction allowed improved load alleviation capability. They showed that in the case of a 25° hinge, a low wingtip mass is beneficial for the flutter speed, while a zero stiffness hinge with a high wingtip mass decreases the flutter speed. Castrichini et al. (2016, 2017a) explored the effect of a passive nonlinear hinge spring to connect the folding wingtip to the main wing. They showed that significant load alleviation was possible when the system has a low overall stiffness around the trim equilibrium point for a large enough range of deflection angles. Moreover, they showed that through proper wingtip design, it is possible to increase the wing aspect ratio with a small increase, or even reduction, of the gust loads experienced by the aircraft. Balatti et al. (2021a) investigated the problem of worst-case gust loads of a simplified aircraft model with elastic wings and hinged wingtips. They performed multi-objective optimisation on the wingtips parameters considering the worst-case gust loads to exploit the wingtips' capability. In Balatti et al. (2021b), the simplified aeroelastic model defined in Balatti et al. (2021a) and a detailed Nastran model were used together for wing gust load identification.

Experimental work has been performed to confirm the ability of hinged wingtips to reduce gust loads. Cheung et al. (2018) conducted a series of steady and dynamic wind tunnel tests using a flared hinged folding wingtip device. They considered both steady and dynamic aerodynamic conditions, in conjunction with variations in the stiffness of the folding hinge. The steady aerodynamic experiments for a stiff-hinge and a free-hinge demonstrated that the folding wingtip is statically aerodynamically stable regardless of hinge stiffness. Moreover, in their study, the predictions by the Nastran aeroelastic models and data from experiments showed similar trends for gust load alleviation performance with respect to changes in hinge spring stiffness for different hinge angles. Furthermore, the achieved reduction from the wind tunnel measurements is higher than predicted. Cheung et al. (2020) added an aerodynamic surface onto the wingtip to control the folding action. In a series of steady aerodynamic tests, they demonstrated that this device could maintain the orientation of the wingtip over a range of wind tunnel velocities and angles of attack. Moreover, they showed that actuating the secondary aerodynamic surface could improve the load alleviation capability already achieved by the folding wingtip alone.

The effects of the bending stiffness, tailoring of the main wing, and the impact of the hinge release instant on the final gust load alleviation of the hinged wingtip, were considered in Carrillo et al. (2022). In that work, the authors found that the linear model overpredicts the flutter speed by more than 40%, and a change in the flutter mechanism is found at different hinge conditions. Contrary to conventional wings, wash-in tailoring increases flutter speed. Moreover, the authors showed no clear relationship between the GLA and the structural properties of the wing, while a notable effect of the hinge release timing on the GLA was found.

In 2017 Wilson et al. (2017) proposed the Semi Aeroelastic Hinge (SAH) concept; the wingtip is kept in a horizontal position during flight to maximise the aerodynamic performance by using a dedicated locking mechanism. When a trigger event is detected, the wingtip is actively released, and it acts as a passive load alleviation system driven only by aerodynamic and inertia forces. When the load event is finished, an actuator returns the wingtip to its original configuration. This concept could allow a substantial increment of the wing-span and a weight-saving opportunity. Castrichini et al. (2018b) showed that the capability of the SAH concept is strongly affected by the timing between the hinge released and the load event. They found that the release time of the wingtip is a crucial parameter for load alleviation. Indeed, they observed a worsening or an improvement of the loads alleviation effects by varying the hinge release delay. An early release of the wingtip is required to obtain the same load alleviation performance as a pure floating hinge aircraft. A series of patents from Airbus followed (Castrichini et al., 2018a; Wilson et al., 2019a, 2021), focusing on devices for moving and controlling a hinged wingtip (Castrichini et al., 2018a; Wilson et al., 2019a) and a method to perform a descent in an aircraft (Castrichini et al., 2018a). Wilson et al. (2021) proposed a device on the hinge to allow the wingtip to switch between flight and load alleviation configurations. During the flight, a restraining assembly ensures the wingtip is fixed. During the gust event, the wingtip could adopt the load alleviation configuration by releasing the restraining force.

In recent years, Airbus developed AlbatrossOne, a basic proof of concept demonstrator for the Semi Aeroelastic Hinge technology. The wing was approximately 1:14 scale of a generic short range aircraft. It was geometrically scaled to represent a future full-scale aircraft, although, it was not dynamically scaled for either handling qualities and/or aeroelasticity in terms of mass and stiffness properties. The wing has five wing tip configurations: a 2.6 m wing span with no wingtips, a 3.2 m wing span with fixed wingtips, a 3.2 m wing span with the wingtips free to rotate, a 3.7 m wing span with fixed wingtips, a 3.7 m wing span with the wingtips free to rotate. Flight testing showed that the wingtips were statically and dynamically stable throughout the flight. Furthermore, the wing load alleviation effect from the free

wingtips has been confirmed through different flights (Wilson et al., 2019b). Healy et al. (2022) described a novel flight test method for a UAV constrained by a tether, resulting in steady, controlled, elliptical flight paths. The authors applied this technique to the AlbatrosONE and characterised the effect of sideslip on the equilibrium position of free-floating hinged wingtips. This innovative approach allowed the boundaries of the flight envelope to be determined safely to verify the stability boundary of such a device.

The nonlinear effect of hinged wingtips was considered by Conti et al. (2021). They investigated the effects of geometric nonlinearities on the quasi-steady aeroelastic response of an aircraft with hinged wingtips. They showed that in the case of a high angle of attack, the wingtip response could vary significantly when geometric nonlinearities are accounted for; however, a negligible impact was observed on the main airframe structure. Moreover, nonzero sideslip affects the effective flare angle leading to an asymmetric stiffness between the left and right hinge.

Different authors considered the handling qualities of aircraft with hinged wingtips. Castrichini et al. (2020) showed that regardless of the 25% increment in span, a free-hinge aircraft has the same handling qualities and dynamic response of the baseline model with no wingtip extension. The authors suggested that the hinged wingtips could be used both as a load alleviation device and to alleviate the roll-damping increment induced by the longer span. Moreover, this increases the aileron authority and a consequent weight-saving with respect to the fixed-hinge aircraft that required a bigger aileron size. Ajaj (Ajaj, 2021) confirmed that the introduction of the hinged wingtips has a minor influence on the handling qualities regardless of the flare angle, fold angle, and wingtip size to the case of no extension. Moreover, he showed that the effects were on the phugoid mode improving the damping due to the increased drag at large fold angles, and the time constant for the spiral mode significantly reduces, making this mode more stable. Sanghi et al. (2023) considered a very flexible, high-aspect-ratio-wing transport aircraft with hinged wingtips and different control surfaces inboard and outboard of the hinge. They showed that at low dynamic pressure, free-hinged wingtips do not impact the roll manoeuvre due to inboard-of-hinge control surfaces, while at higher dynamic pressure, they make the aircraft roll slower. Moreover, for roll manoeuvres due to control surfaces on the wingtip, with both free and fixed hinges, the aircraft experienced reversal and the free hinged experienced limit-cycle-oscillations. Free-hinged wingtips aircraft roll angles and rates were higher for manoeuvres controlled by the trailing edge control surfaces inboard-of-hinge but slower than those imposed by the corresponding control surface on the wingtip.

The unsteady nature of a gust and strong coupling between the resulting aerodynamic loads and structural deformations make the modelling process quite complex. Hence numerical models have to be validated. This work presents the design of a wing and fixed and hinged 3D-printed wingtips, called basic wingtips, the model structural characterisation, wind tunnel tests and model validation. Static and dynamic wind tunnel tests were performed to prove the load alleviation concept and validate the aeroelastic models. The numerical models developed were based on the detailed model used in Balatti et al. (2021b). The validated numerical models of the wing with the basic wingtips suggested that wingtip weight reduction could increase load alleviation performance. Moreover, based on the validated models of the wing with the basic wingtips, numerical simulations of light wingtips are considered, and numerical and experimental tests with a hybrid wingtip are performed. The hybrid wingtip was manufactured with two materials to shift its centre of mass closer to the hinge. Moreover, a sensitivity analysis identified the effects of different wingtip parameters on the gust load alleviation performance of wings with hinged wingtips. The present paper is organised as follows. In Section 2, the design of the wing with a fixed wingtip and two hinged wingtips (basic wingtips) and the experimental setup are give. In Section 3, the aeroelastic models are introduced. In Section 4, the structural characterisation of the wing with the basic wingtips are given. In Section 5, the results of static and dynamic wind tunnel tests are reported. In Section 6, the comparison between gust responses computed by the aeroelastic models and gust responses measured experimentally are presented. Based on the validated models of Section 6, a numerical analysis of a light wingtip, the numerical and experimental investigation of the hybrid wingtip and the wingtip weight investigation are performed in Section 7 before the conclusions are presented.

2. Wing and wingtips design and experimental setup

To experimentally prove the beneficiary effect of the hinged wingtip device and validate aeroelastic models, a straight untapered half-wing with a 1 m span and 0.134 m chord able to accommodate different wingtips was designed and manufactured. The wing comprises a 780 mm long aluminium spar with an 'cross-shaped' cross-section and 3D-printed aerofoils connected to the spar (Balatti et al., 2022b). The cross-section was selected to independently increase the in-plane and out-of-plane wing structural frequencies.

To minimise the wing thickness but allow the introduction of an aluminium spar, the constant wing profile selected is the NACA0015 profile. Eight identical 3D-printed aerofoils are connected along the spar's span through two pairs of bolts and washers. The spar's tip is used to connect the wingtips through four pairs of bolts and washers. This design was selected to suit different wingtips without changing the rest of the wing. Figs. 1(a)–1(c) show the manufactured spar, the spar internal cross-section and one of the 3D-printed sections.

Three wingtips (basic wingtips) with the same span and weight were manufactured with 3D-printed material. The first wingtip is fixed, while in the other two, there is a hinge with an angle with respect to the free stream velocity (flare angle). To ensure a high flutter speed (Balatti et al., 2021a), in both cases, the flare angle was set to 10°. The hinge location is at 80% of the total wingspan. A 0.35 mm $\times$ 25 mm $\times$ 100 mm metal plate connects the wingtip root to the

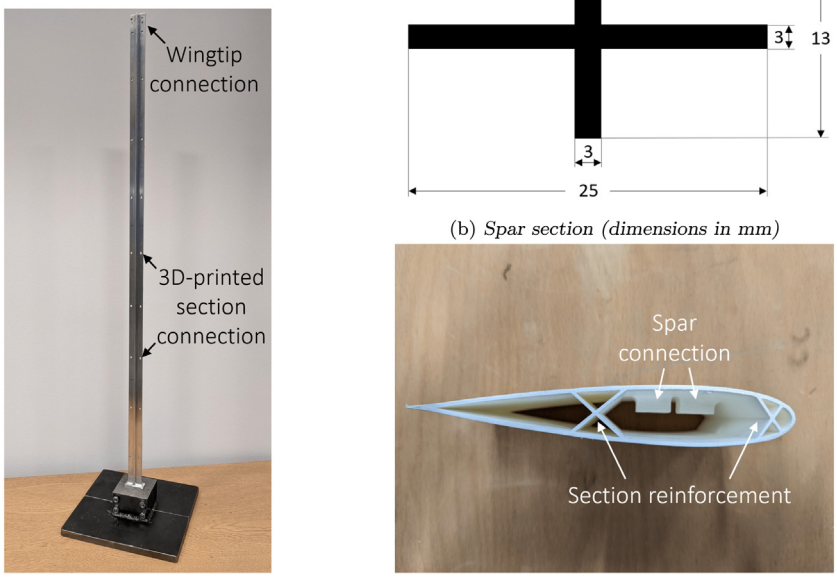

(a) *Spar manufactured* (b) *Spar section (dimensions in mm)* (c) *Top view*

Fig. 1. Aluminium spar and aerofoil section.

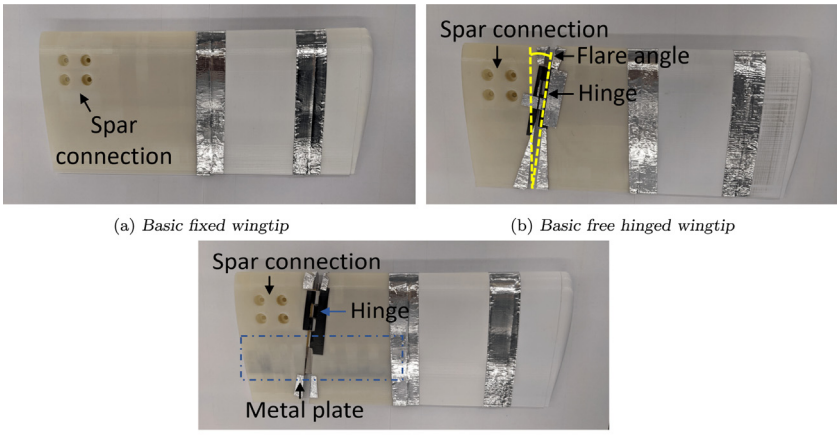

(a) *Basic fixed wingtip* (b) *Basic free hinged wingtip*

(c) *Basic hinged wingtip with torsional spring*

Fig. 2. Basic wingtips.

main wing in one of the two hinged wingtips to introduce a torsional stiffness at the hinge. Fig. 2 shows the fixed and the hinged wingtips. Table 1 gives the weight of the wing components. Due to the accuracy of the 3D-printer, the mass of the 3D-printed sections varies between a minimum value of 54.3 g and a maximum of 56.4 g. For the aeroelastic model, the average value of 55.2 g was used. The wingtip assembly comprises the section connected to the spar (40 g), the hinge (3.8 g) and the wingtip.

The 3D-printed sections were manufactured in the laboratory of Swansea University by using two different materials: PLA and ABS-M30. For printing, each material requires a specific machine. 3D-printing using ABS-M30 is more time-consuming but allows higher accuracy with respect to PLA. Due to the high precision required in manufacturing the hinge

Table 1
Mass of wing components with the basic wingtip.

Component	Mass [g]
Spar	292.0
Pair of bolt and washer	1.9
Wing 3D-printed section	55.2
Wingtip bearings and shaft	3.8
Wingtip threaded bar	13.0
Metal plate	≈0
Wingtip assembly	193.8

case, ABS-M30 has been used. For consistency, the corresponding section for the fixed wingtip has also been 3D-printed using ABS-M30. All the other parts have been 3D-printed using PLA.

2.1. Experimental setup

The structural, aerodynamic and aeroelastic characterisation of a wing is performed using different sensors and equipment depending on the information to be extracted. Accelerometers were used for the impact hammer test, and a laser displacement sensor was used to record the fold angle free oscillation response from which the wingtip natural frequency and damping ratio were measured. Moreover, laser displacement sensors were used in the wind tunnel tests to measure the vertical displacement of specific points. A six-component force balance was used for the measurement of the wing root loads.

Impact hammer tests were performed using the Data Physics Abacus 901 dynamic signal analyser and accelerometers to identify mode shapes, natural frequencies and damping ratios. The accelerometers PCB 352C03 and PCB-352C22 were used. Accelerometers can be considered as concentrated masses at their actual positions.

Three LK-G507 Precision 1D Laser Triangulation sensors have been used in the wind tunnel. The LK-G507 Precision 1D Laser Triangulation sensor can measure the distance of objects between 250 mm and 1000 mm from the laser with an accuracy of ± 500 μm and a sampling frequency up to 1 GHz. The laser displacement sensors were also used to identify the hinge fold angle by measuring the absolute vertical displacement of a point on the hinge and a point on the wingtip. The rotation at the tip of the wing due to bending was neglected as it was found to be negligible. A National Instrument NI-9231 module is used to record the sensor output voltages. The NI-9231 has eight analogue input channels, with 24 Bit resolution and ± 5 V range and is connected to the cDAQ-9189. The cDAQ-9189 is a CompactDAQ Ethernet chassis for distributed sensor measurement systems.

The Swansea University wind tunnel is equipped with an AMTI GEN 5, a six-component force balance able to measure wing root forces and moments. Moreover, the balance can rotate to impose different wing root angles of attack. The balance has signal conditioning with a 1 kHz anti-aliasing filter, oversampling and digital signal processing. Each of the six analogue output channels has an independent 16-bit DAC conditioned by a low-pass reconstruction filter and amplifier. Each channel has a configurable gain to select the measurable maximum and minimum level load. Before and after each experiment, for all of the AoA considered during the test, measurements of the wing root loads were performed without any airspeed. These values were used to separate the aerodynamic loads from the loads due to gravity.

Atmospheric disturbance models are categorised into two idealised categories: discrete gusts and continuous turbulence (European Aviation Safety Agency, 2020). Due to its shape, a discrete gust is typically called a '1 - cosine' gust. The profile is defined as

$$w_g(t) = \begin{cases} \frac{w_{g_0}}{2}\left[1 - \cos\left(2\pi \frac{V}{l_g} t\right)\right] & \text{for} \quad 0 \le t \le \frac{l_g}{V} \\ 0 & \text{for} \quad t > \frac{l_g}{V} \end{cases} \tag{1}$$

where w_{g_0} is the maximum gust velocity and l_g is the gust wavelength. According to the European Aviation Safety Agency (EASA) regulation (European Aviation Safety Agency, 2020) for the case of civil, commercial aircraft, gust wavelengths are varied between 18 m to 214 m, and the gust velocity is calculated as

$$w_{g0} = w_{ref}\left(\frac{H}{106.14}\right)^{1.6} \tag{2}$$

where the gust gradient H is half the gust wavelength l_g and the reference gust velocity w_{ref} reduces linearly from 17.07 m/s Equivalent Air Speed (EAS) at sea level to 13.41 m/s EAS at 4572 m, and then again to 6.36 m/s EAS at 18288 m.

The experimental generation of discrete gusts in the wind tunnel is a complex task and requires specific equipment in the wind tunnel (Balatti et al., 2022a). In Balatti et al. (2022a), the design, installation, and commissioning of a gust generator in the Swansea University wind tunnel was described. Discrete gusts, according to EASA, are described in terms of l_g and w_{g_0} as in Eq. (1) while in Balatti et al. (2022a) gusts have been defined in terms of the maximum vane rotation and the frequency of the '1 - cosine' function. Indeed, the maximum vane rotation is proportional to the maximum gust

Table 2
Convergence study on the structural model of the spar.

	Number of elements				
	10	20	40	100	200
Mode 1 [Hz]	9.8	9.8	9.8	9.8	9.8
Mode 2 [Hz]	60.5	61.4	61.6	61.6	61.6
Mode 3 [Hz]	167.0	171.1	171.1	172.3	172.3
Mode 4 [Hz]	239.9	240.1	240.1	240.2	240.2

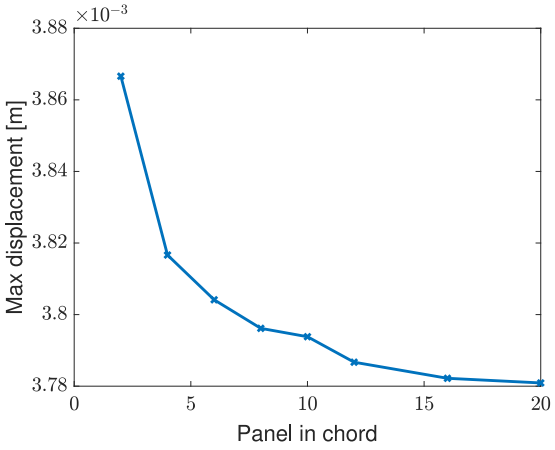

Fig. 3. Convergence of the aerodynamic model of the wing with fixed wingtip.

amplitude (w_{g0}) and the frequency of the '1 - cosine' function is inversely proportional to the gust length (l_g). From the frequency of the '1 - cosine' function, l_g may be calculated from

$$\frac{V}{l_g} = f \tag{3}$$

Discrete gusts have been obtained using the vane rotation defined after the parametric study considering $A = 5°$, $A = 10°$ and $A = 15°$ (Balatti et al., 2022a). In this work, gusts produced by the three vane rotations are called small, medium and large discrete gusts (e.g. for $l_g = 1.8$ m, vertical gusts of 0.24 m/s, 0.46 m/s, and 0.63 m/s).

3. Numerical model

The aeroelastic model representative of the manufactured wing with the fixed wingtip was developed in Nastran. Nastran has been widely used to model aeroelastic systems and for modelling wings with hinged wingtips (Castrichini et al., 2016, 2017a, 2018b; Castrichini, 2017). The aluminium spar was modelled using beam elements. A convergence study was performed to assess the number of elements required to model the beam. A model with 200 elements was considered as a reference, and the first five natural frequencies were considered in each case. The convergence study terminated when there was no difference between the model predictions and the reference, up to the first decimal point. The first four modes were considered because the fourth mode is the first torsional mode. Table 2 reports the results of the convergence study. The model with 100 elements was considered for the gust response, although the model with 20 elements has a maximum error of 1% and gives similar results. The weight and inertia of each 3D-printed wing and wingtip section and the metal bar were modelled as concentrated masses with their correct inertia at their actual position. Inertia and centre of mass position were calculated by Solidworks by correcting the mass density to match the weight of each manufactured part. To consider the joint flexibility, each concentrated mass was connected to the spar through a rigid beam and a spring via a CBUSH element. The Doublet Lattice Method (DLM) was used to model the aerodynamic forces and only quadratic aerodynamic panels were considered. After a convergence study was performed considering the maximum tip vertical displacement due to a gust, 20 panels in chord and 150 panels in span were used. Fig. 3 shows the results of the convergence study. The convergence study was not performed independently in the spanwise direction because only square panels were considered. The selection of the panels' dimensions was not based on the maximum frequency of interest because, in this case, it overestimated their dimensions.

From this aeroelastic model, two aeroelastic models representative of the wing with the two basic hinged wingtips were obtained introducing a hinge at 80% of the wing span and with a fold angle of 10°. The hinge was modelled as two coincident nodes connected via a CBUSH element with the coordinate system aligned to the hinge axis. In addition, a

Table 3
Summary of the Nastran model.

Nodes	176
Beam elements	100
Concentrated masses	35
Rigid beams	56
Spring elements	14
Aerodynamic panels	3000

Table 4
First five structural natural frequencies and damping ratios of the spar measured experimentally and calculated from the model (OOP: out-of-plane)

Measured [Hz]	Calculated [Hz]	Error	Damping ratio [%]	Mode shape
9.8	9.8	0	0.1	1st OOP bending
62.0	60.2	3.0%	0.1	2nd OOP bending
175.0	169.4	3.3%	0.05	3rd OOP bending
258.1	245.5	5.1%	0.07	1st Torsion
344.8	332.8	3.6%	1.0	4th OOP bending

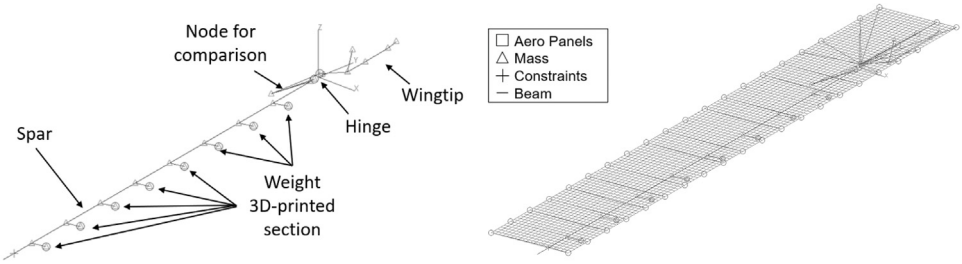

(a) *Structural model* (b) *Aeroelastic model*

Fig. 4. Nastran model.

PBUSH element introduced the stiffness at the hinge. The aerodynamic model was divided into two sections, the main wing section, from the wing root to the hinge, and the wingtip section, from the hinge to the tip (Castrichini, 2017). Following the procedure used in the case of the wing with a fixed wingtip, a convergence study was performed to assess the number of panels required to model each section, considering only square panels. As a result of the convergence study, 20 panels in chord were used for both sections. A total of 2400 aerodynamics panels were used to model the main wing, and 600 aerodynamics panels for the wingtip. Table 3 summarises the model and Fig. 4 shows the wing structural and aerodynamic models. Fig. 4 also shows the position of the node on the spar at 0.78 m from the wing root used to compare numerical and experimental time responses. Moreover, it shows the wingtip masses at their centre of mass positions.

4. Spar and wing structural characterisation

Impact hammer tests were performed separately on the spar and the wing, considering all the wingtips, to assess their structural natural frequencies, mode shapes and damping ratios. Each Frequency Response Function (FRF) was calculated by the dynamic signal analyser, taking the average from ten repetitions. The FRFs post-processing was performed in Matlab using the built-in function 'modalfit' to extract natural frequencies, damping ratio and modes shapes. The information extracted from the structural characterisation was used for the model validation. In each test, the impact force was applied at the accelerometers' position on the opposite side of the airfoil with respect to the sensor's location. Moreover, impact hammer tests were performed on the wing to ensure all the parts were well connected and the FRFs were demonstrated reciprocity. First hammer tests were performed to measure the first natural frequency of the 3D-printed sections that will be bolted along the wing. Their first natural frequency is 211 Hz.

Secondly, the impact hammer test on the spar was performed using three PCB-352C22 accelerometers and one PCB 352C03 accelerometer uniformly distributed along the spar span. Fig. 5 shows the test setup of the spar. Table 4 reports the identified structural natural frequencies below 500 Hz and the corresponding mode shapes of the spar.

Finally, impact hammer tests were performed on the wing considering the three wingtips and using four PCB-352C22 accelerometers uniformly distributed along the wingspan and at the spar location. The wing was hung vertically with the wing root at the top to ensure the wingtip was parallel to the main wing. Fig. 6 shows the impact hammer test setup in the cases considered. The excitation force was not applied at the fourth accelerometer location because, in the hinge cases, the high flexibility and low inertia made the excitation challenging. In the identified FRFs the main peaks are identifiable and the cross FRFs confirm reciprocity, i.e. the system is linear.

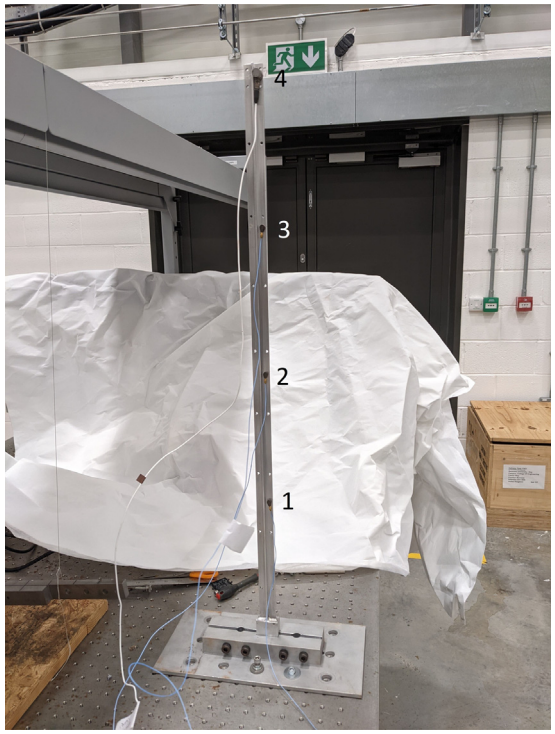

Fig. 5. Spar impact hammer test.

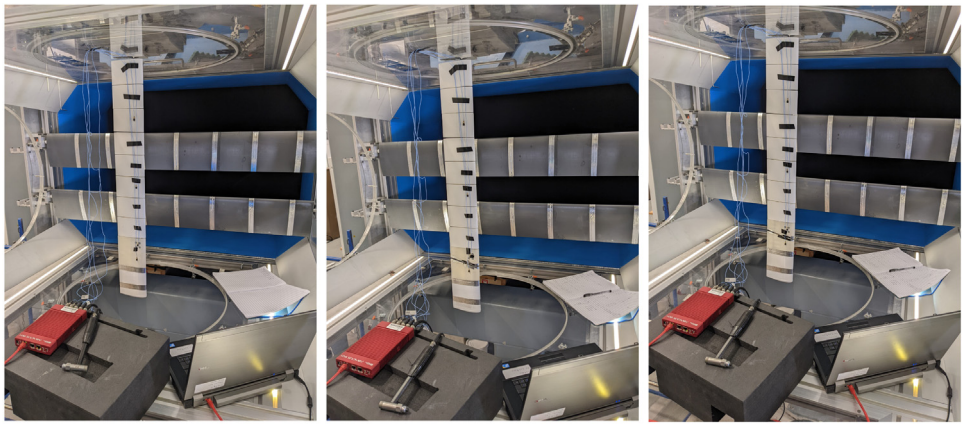

(a) *Fixed wingtip* (b) *Free hinged wingtip* (c) *Hinged wingtip with torsional spring*

Fig. 6. Impact hammer test set up of the wing with different wingtips.

Light accelerometers are not suitable to measure low frequency components. Hence, to identify the hinged wingtip's natural frequency and damping ratio, a laser was used to record the time history of vibration of a point on the wingtip when the wingtip was subjected to an initial displacement. Using the peak-to-peak and logarithmic decrement methods, the natural frequency and damping ratio in both cases were identified. Table 5 reports the measured structural natural frequencies below 50 Hz and the corresponding damping ratios of the wing with the different wingtips. The first natural frequency of the wing with the free hinged wingtip is not zero due to the gravitational effect. The metal plate on the hinge increases the wingtip's natural frequency by 0.2 Hz and decreases the damping ratio by a factor of four. Due to the presence of the hinge and the consequent reduction in the main wing length, the natural frequency of the first out-of-plane bending mode increases from 3.5 Hz (fixed wingtip) to 4.9 Hz in the case of the free hinged wingtip and 5.1 Hz in the case of the hinged wingtip with the torsional spring.

Table 5
Structural natural frequencies below 50 Hz and damping ratios of the wing with the different basic wingtips measured experimentally and calculated from the models.

Fixed Wingtip				Hinged wingtip			
Measured [Hz]	Calculated [Hz]	Error [%]	Damping ratio [%]	Measured [Hz]	Calculated [Hz]	Error [%]	Damping Ratio [%]
3.5	3.5	0	0.4	1.2	1.2	0	2.7
19.6	19.7	0.5	1.7	4.9	5.0	2.0	1.8
23.4	22.1	5.6	0.8	22.1	20.3	8.1	0.3
49.6	47.8	3.6	0.7	29.6	30.8	4.1	0.6

Hinged wingtip with torsional spring			
Measured [Hz]	Calculated [Hz]	Error [%]	Damping ratio [%]
1.4	1.4	0	0.7
5.1	5.1	0	3.5
21.0	20.3	3.3	2.3
29.1	30.6	5.2	0.8
49.5	46.9	5.3	1.3

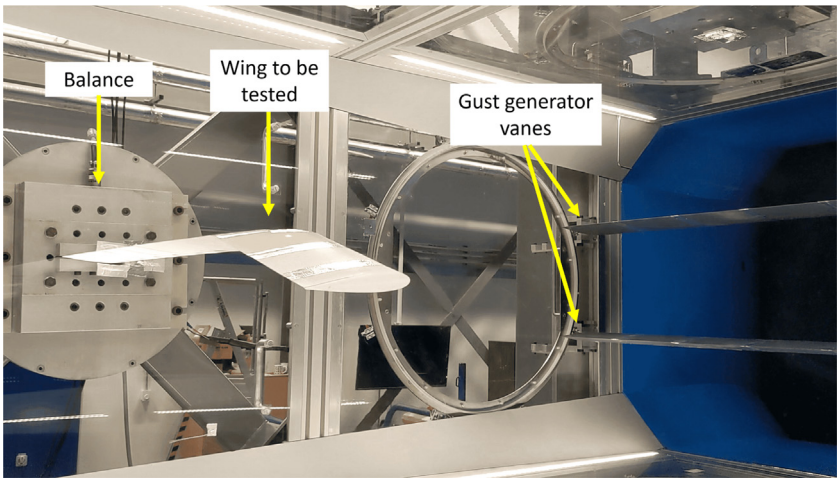

Fig. 7. Wing installed in the wind tunnel.

5. Wind tunnel tests

Static and dynamic wind tunnel tests were performed to assess the static and dynamic performance of the wing with the manufactured wingtips. The wing root was connected to the six-component force balance to record the wing root loads. The wind tunnel was equipped with the gust generator to produce discrete gusts (Balatti et al., 2022a) and three LK-G507 Precision 1D Lasers. Fig. 7 shows the wing installed in the Swansea University wind tunnel, the balance and the gust generator.

5.1. Static test

A static wind tunnel test was performed, changing the wing root angle of attack (AoA) from 0° to 12° to −12° and back to 0° with increments of 1°, recording with a sampling rate of 300 Hz for 20 s. Tests were performed at airspeeds of 10 m/s, 14 m/s, 18 m/s and 22 m/s, which corresponds to a Reynolds number in the range of $1.6{\cdot}10^5$ to $3.6{\cdot}10^5$ considering the wing chord as characteristic length. The wing performance was considered in terms of nondimensionalised force and moment coefficients. The nondimensionalization was performed considering a constant value for the wing dimension to ensure that a reduction in wing span, e.g. due to a significant wingtip rotation, did not increase the nondimensionalization coefficient.

From the measured lift, L, the lift coefficient C_L has been calculated as

$$C_L = \frac{L}{0.5\rho V^2 S} \tag{4}$$

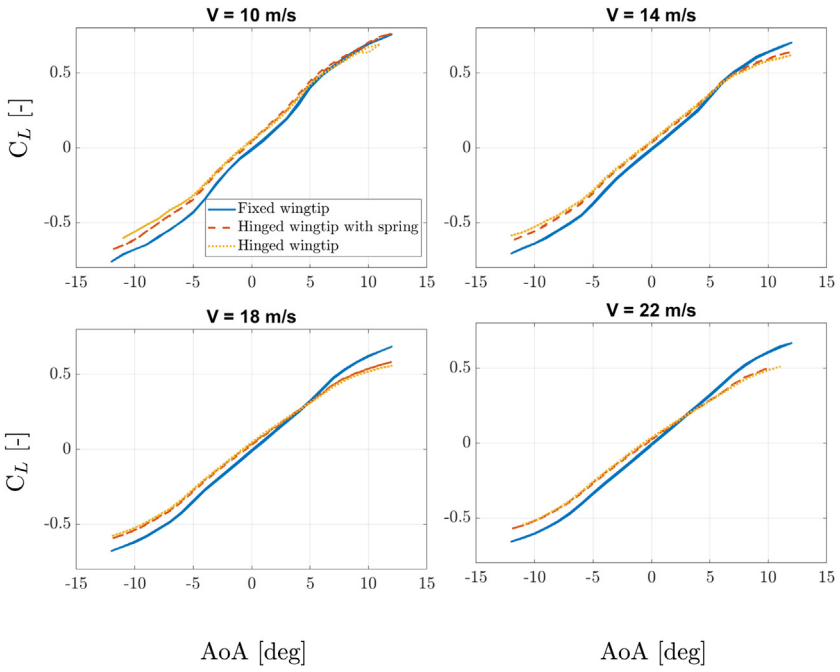

Fig. 8. Lift coefficient at different angles of attack and airspeeds for the wing with the basic wingtips.

where ρ is the air density calculated from the air temperature, V is the recorded free stream velocity, and S is the wing surface area given as 0.134 m^2. Fig. 8 shows the C_L values at different AoA for the wing with the different wingtips.

The C_L curve of the wing with the free hinged wingtip and the one with the hinged wingtip and a torsional spring have a similar trend. Indeed, Table 5 reports that the spring on the hinge only slightly modifies the natural frequencies due to its low stiffness. The C_L curve of the wing with a fixed wingtip and the one with a free wingtip intersect, representing the AoA for which the wingtip is parallel to the main wing. Fig. 9 shows the intersection of the lift coefficient curves and define the intersection point as threshold. Indeed, Wing Root AoAs (WRAoAs) smaller than the threshold are associated with a negative fold angle (wingtip fold-down), and WRAoAs greater than the threshold are associated with a positive fold angle (wingtip fold-up). When the wingtip is folded-down, the wingtip AoA is higher than that of the main wing and vice-versa when the wingtip is folded-up. Increasing the airspeed, the AoA for which the wingtip is parallel to the main wing decreases. Indeed, for the same AoA and increasing airspeed, the lift produced is higher; consequently, for a lower AoA, the wingtip can produce a lift able to balance its weight. For AoAs smaller than the threshold, the lift produced by a wing with a hinged wingtip is higher than the lift produced by a similar wing with a fixed wingtip due to the extra lift produced by the wingtip folded down. AoAs greater than the threshold are associated with higher lift for the wing with a fixed wingtip with respect to the wing with a hinged wingtip because the wingtip folded up produces less lift.

From the measured wing root out-of-plane bending moment, M_{WRBM}, the rolling moment coefficient C_R has been calculated as

$$C_R = \frac{M_{WRBM}}{0.5\rho V^2 S s} \tag{5}$$

where s is the wingspan. Fig. 10 shows the rolling moment coefficient values at different AoA for the wing considered with all the wingtips. As in the case of the C_L curves, the C_R of the wing with a fixed wingtip and the one with a hinged wingtip intersect.

Figs. 8 and 10 show that the slope of the C_L-AoA and C_R-AoA curves for the wing with a hinged wingtip is lower with respect to the wing with a fixed wingtip. Gusts loads are dynamic events where the response depends on the interaction of aerodynamic, inertia and elastic loads. As a first approximation, they can be seen as a static event where gusts produce an increment of the wing AoA, which causes an increment in lift. So, an AoA increment produces a smaller increment in lift and wing root out-of-plane bending moment in the wing with a hinged wingtip when compared to the wing with a fixed wingtip. Consequently, gusts cause a smaller load increment in the case of a wing with a hinged wingtip compared to a wing with a fixed wingtip. These results are in accordance with the literature and confirm the ability of a hinged wingtip to reduce gust loads (Cheung et al., 2018).

Fig. 11 shows the C_R and C_L curve plotted one against the other to compare the performance of the wingtips considered. As with the $C_L - \alpha$ curves, the $C_L - C_R$ also intersects. For C_L values lower than the point of intersection, C_R is higher for the hinged wings and vice versa.

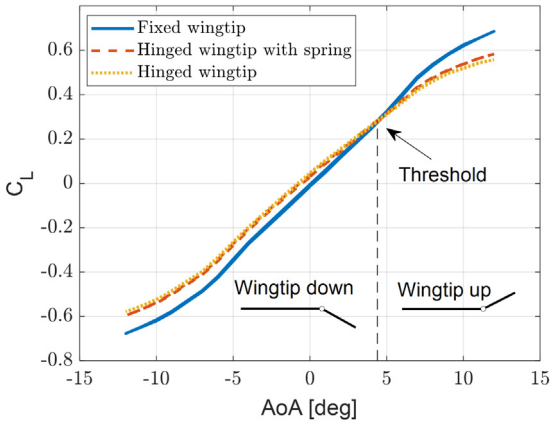

Fig. 9. Lift coefficient at different angles of attack and 18 m/s.

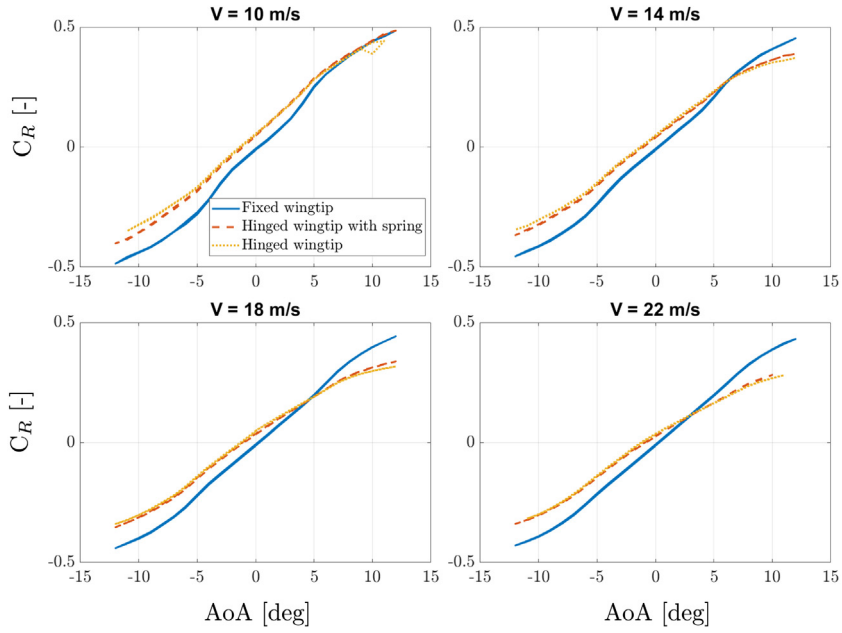

Fig. 10. Rolling moment coefficient at different angles of attack and airspeeds for the wing with the basic wingtips.

Fig. 12 shows the fold angle for different AoA and airspeeds of 14 m/s, 18 m/s and 22 m/s. The identified fold angle from the measurements at 10 m/s is not reliable because at 10 m/s the lift produced is not enough to balance the weight. Indeed, the calibration has been performed keeping the wing straight. For low AoA and airspeed, the wingtip is not producing enough lift to balance the weight, and its fold angle is $-27°$, the minimum negative angle achievable by the hinge. At low airspeed, the spring on the hinge produces a moment that contributes to the wingtip rotation. Increasing the airspeed, the effect of the spring decreases.

Figs. 8 and 10–12 show that varying the airspeed and the AoA the results are consistent.

5.2. Dynamic test

The wing with all the wingtips has been subjected to discrete gusts with different levels of intensity and gust lengths from 1.29 m to 9 m and an airspeed of 18 m/s, corresponding to the frequency of the '1 - cosine' function from 14 Hz to 2 Hz (corresponding to the reduced frequency from 0.3 to 0.05), respectively. To evaluate the effect of the WRAoA, the gust response was performed at WRAoAs of 2°, 4.4° and 6°. Linear interpolation was performed on the C_L values at 18 m/s to find the WRAoA for which the hinged wingtip was parallel to the rest of the wing, and was estimated at 4.4°. A WRAoA of 2° was considered to ensure that during the gust response, any wingtip rotation was not reaching the lower

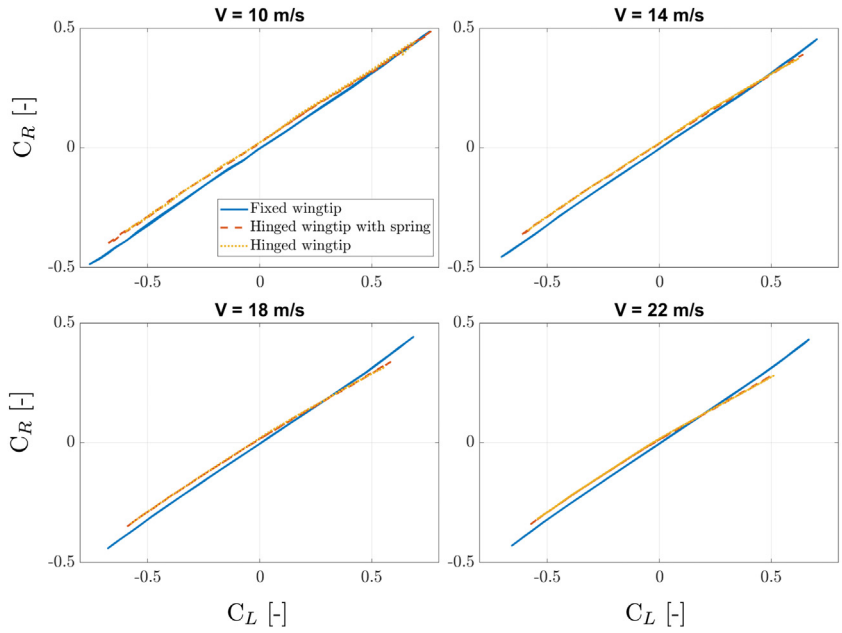

Fig. 11. Rolling moment coefficient variation with lift coefficient at different airspeeds for the wing with the basic wingtips.

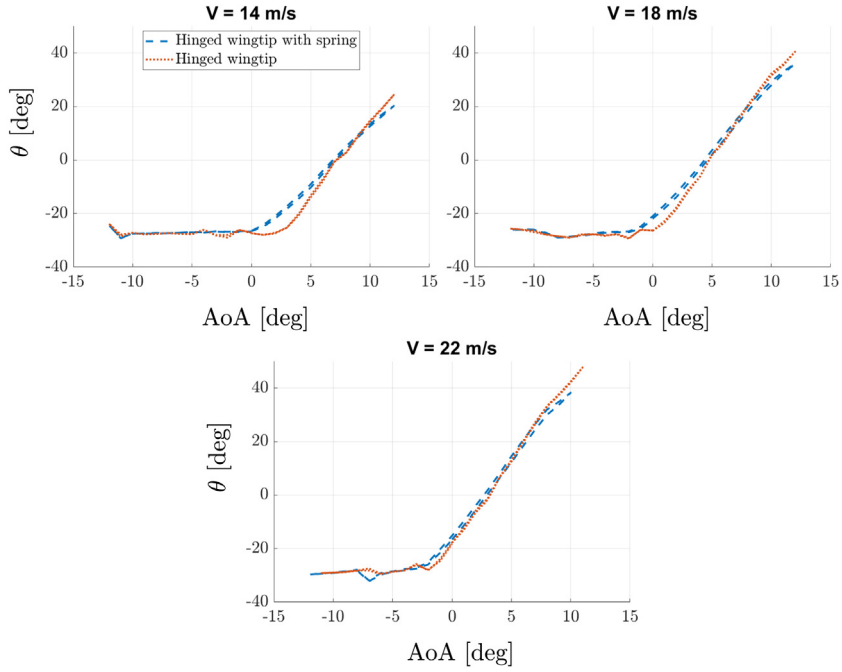

Fig. 12. Wingtip fold angle at different angles of attack and airspeeds for the wing with the basic wingtips.

hinge rotation limit. A WRAoA of 6° was considered to ensure that before the gust the wing with a hinged wingtip had a lower Wing Root Bending Moment (WRBM) with respect to the fixed wingtip.

Fig. 13 shows the results of the same gust response repeated three times. In the three cases, the measurements are very similar showing a good repeatability.

Fig. 14 shows the measured time history gust response of the WRBM and fold angle for the medium gust amplitude and the selected WRAoAs. Increasing the WRAoA shows that the WRBM before the gust increases more for the wing with the fixed wingtip with respect to the free-hinged wingtip. Moreover, increasing the WRAoA, the hinge spring contribution

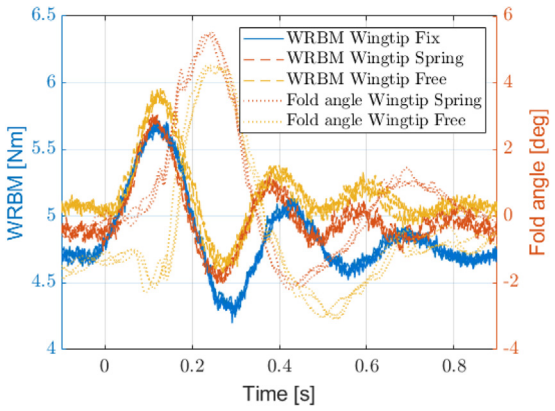

Fig. 13. Typical gust response, where each measurement is repeated three times to evaluate repeatability (gust length 9 m), WRAoA 4.4° for the wing with the basic wingtips.

decreases, and the WRBM and fold angle gust response in the case of the free-hinged wingtip become similar to the case of the hinged wingtip with a torsional spring. The gust with the lowest gust length excites the wing torsional mode. Before the gust, the WRBM of the wing with a hinged wingtip is higher than for the fixed wingtip for WRAoAs of 2° and 4.4° and lower for a WRAoA of 6°, in accordance with Fig. 8. Indeed, before the gust, the wingtip is folded down in the cases of WRAoAs 2° and 4.4° and folded up for a WRAoA of 6°. When the gust reaches the wing, the WRBM increases for all the wingtips considered. For the shortest discrete gusts, the wingtip starts to rotate when the WRBM reaches its maximum value and increasing the gust length, the delay between WRBM and fold angle decreases. Indeed, in all the cases, the first negative peak is amplified by the wingtip folded up with respect to the case of the fixed wingtip.

For all tests considered, Fig. 15 shows the maximum and minimum WRBM increment from the trim value due to the gust for all the gusts considered. For a WRAoA of 2°, a free hinged wingtip is able to alleviate the maximum WRBM peaks for all the discrete gusts, except for a discrete gust of 4.5 m. In the same configurations, the wing with a hinged wingtip and torsional spring has performance in between the case of wing with free hinged wingtip and fixed wingtip, except for the case of 4.5 m gust length, where its maximum WRBM is amplified. A similar conclusion can be drawn in the case of WRAoAs of 4.4° and 6° for the small gust, with the difference that in the case of a WRAoA of 4.4°, the WRBM maximum peak for a discrete gust of 4.5 m is higher in the case of the free hinged wingtip with respect to the hinged wingtip with torsional spring and in the case of a WRAoA of 6°, the WRBM maximum peak for a discrete gust of 1.5 m, 3 m and 4.5 m is higher in the case of the hinged wingtip with the torsional spring with respect to the fixed wingtip.

For medium and large discrete gusts and WRAoAs of 4.4° and 6°, the maximum peaks of the WRBM for the wing with a hinged wingtip have similar or higher values compared to the wing with a fixed wingtip. In all the cases, a hinged wingtip alleviates the maximum peak of the WRBM for a discrete gust with a gust length of 9 m. Indeed, in this case, the wingtip starts to rotate before the WRBM reaches its maximum value. In all cases but one, the hinged wingtip amplifies the negative peak. Indeed, Fig. 14 shows that in all the cases, the fold angle reaches its maximum value when the WRBM has its minimum value. So, the hinged wingtip is produces negative lift that decreases the WRBM.

The tested hinged wingtips are able to alleviate the WRBM only for specific gust lengths. Figs. 14 and 15 show that, for all the discrete gusts except for the slowest gust, the hinged wingtip is not reacting fast enough to alleviate the gust loads. In Section 7 the effect of a lighter wingtip is considered.

6. Comparison between experimental and numerical results

Tables 4 and 5 compare the structural natural frequencies measured experimentally and calculated from the dynamic models for the spar alone and the wing with the different wingtips. Moreover, Tables 4 and 5 report the identified structural damping from the impact hammer test, which was introduced in the model. To measure the wingtip's pendulum mode, the impact hammer tests were performed with the wing hung vertically. For the pendulum mode, the structural natural frequencies were calculated considering the pre-load due to the weight.

In the case of only the spar, the first five structural natural frequencies calculated by the model have a maximum error of 5.1%. The good agreement between the numerical model and the experiment is due to the simplicity of the structure analysed. In all the wing cases, the numerical models were tuned to obtain structural natural frequencies similar to the experimental frequencies given in Table 5. To tune the models, an iterative process was performed firstly on the model of the wing with the fixed wingtip, changing the values of the CBUSH elements along the wing and the wingtip. Secondly, the values found were used on the model of the wing with the hinged wingtip to determine the hinge stiffness. In all the cases, the out-of-plane bending and torsional modes were coupled. Indeed, the identification of the torsional modes was possible due to their coupling with the out-of-plane bending mode. For the wing with the fixed wingtip, the first

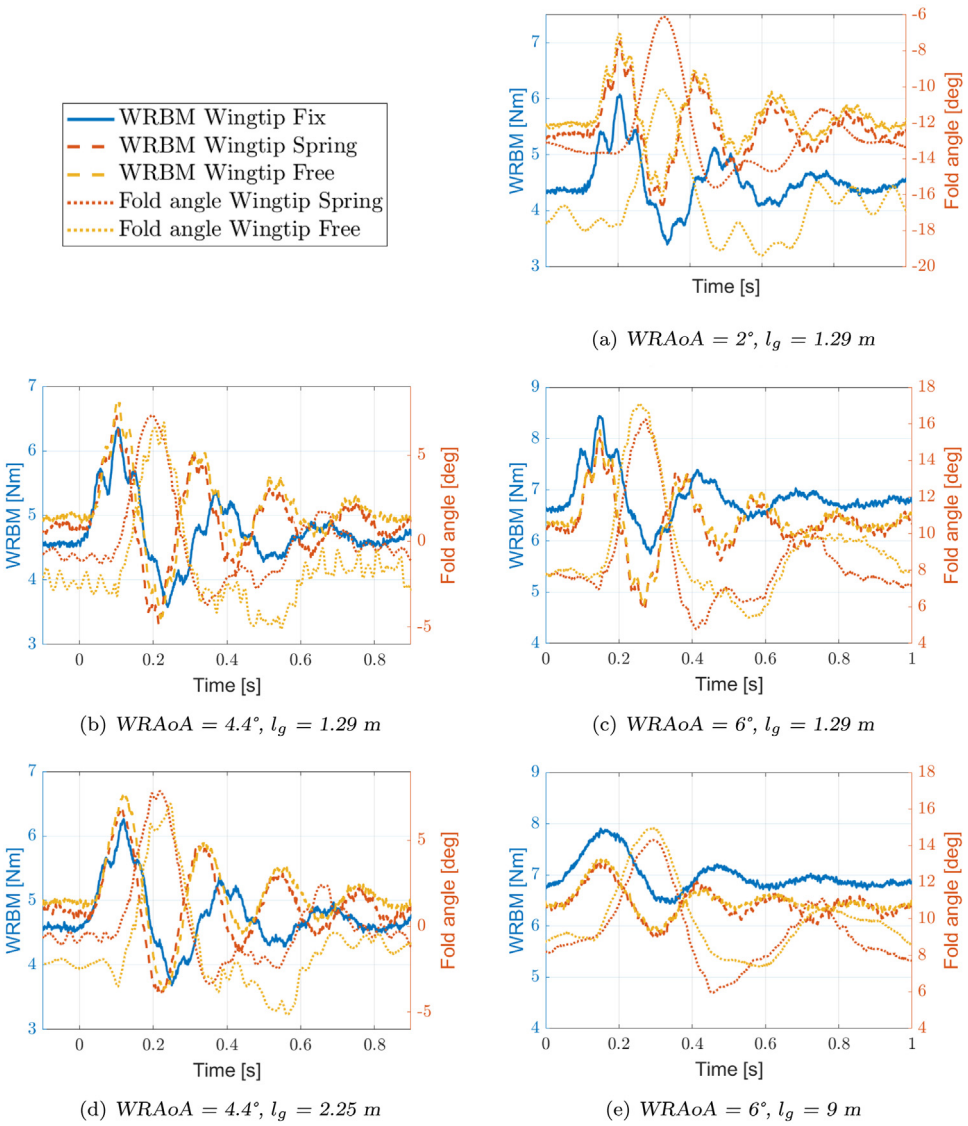

(a) $WRAoA = 2°$, $l_g = 1.29\ m$

(b) $WRAoA = 4.4°$, $l_g = 1.29\ m$

(c) $WRAoA = 6°$, $l_g = 1.29\ m$

(d) $WRAoA = 4.4°$, $l_g = 2.25\ m$

(e) $WRAoA = 6°$, $l_g = 9\ m$

Fig. 14. Wing root bending moment gust response for the wing with the basic fixed wingtip, basic hinged wingtip and basic hinged wingtip with torsional spring and fold angle time history. Medium discrete gust amplitude at different gust lengths and WRAoAs 2°, 4.4° and 6°.

natural frequency is associated with the first out-of-plane bending mode, the second natural frequency is associated with the wing torsion, and the higher natural frequencies have contributions from both out-of-plane bending and torsion. For the wing with the hinged wingtip, the first natural frequency is associated with the wingtip mode, the second natural frequency is associated with the first out-of-plane bending mode, the third natural frequency is associated with the wing torsion, and the higher natural frequencies have contributions from both out-of-plane bending and torsion. In this case, a good match of the first natural frequency was obtained by introducing a suitable spring stiffness in the hinge.

6.1. Comparison gust responses

The numerical and experimental results were compared in terms of gust time history responses of the WRBM, vertical displacement of a point on the wing at 0.78 m from the wing root and hinge rotation. In the model, due to the model linearity, the gust response is not affected by the WRAoA. All the quantities of interest were compared in terms of the increment due to the gust. The numerical gust responses were obtained considering as gust input the respective gust time history measured in Balatti et al. (2022a).

Fig. 16 shows the comparison between the numerical and experimental gust response in the case of the fixed wingtip, Figs. 16(a) and 16(b), the hinged wingtip with torsional spring, Figs. 16(c) and 16(d), and the free hinged wingtip,

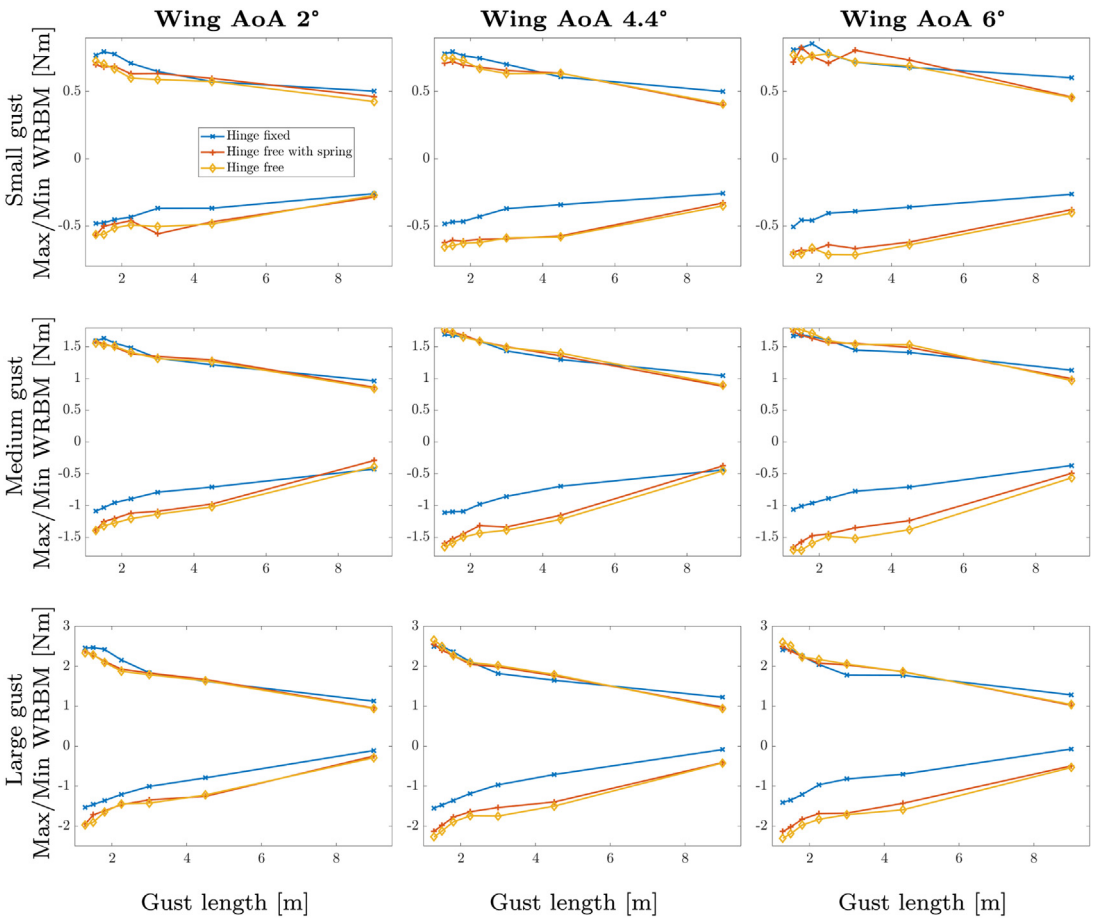

Fig. 15. Wing root bending moment maximum peaks for all the cases considered for the wing with the basic wingtips.

Figs. 16(e) and 16(f). Due to the record of the gust time history, the numerical model correctly predicts the oscillations before the main gust caused by the gust generator starting vortex (Balatti et al., 2022a). Moreover, the maximum peak prediction was correct for all the variables monitored. In the case of the wing with the fixed wingtip, the three experimental results have a similar time response in both quantities of interest and the model correctly predicts them. However, the WRBM has a high-frequency oscillation at around 18 Hz with respect to the experimental results, suggesting lower aerodynamic torsional damping in the model than in the experiment. Furthermore, Figs. 16(d) and 16(f) show that the first effect due to the gust was a slight negative fold angle. Indeed, when the gust reaches the wing, the wing moves vertically, and the wingtip does not move, producing the negative fold angle, which can also be seen in Fig. 14.

The results of the wing with both hinged wingtips have a similar trend and will be commented on together. The experimental results in the case of the wing with hinged wingtips are more affected by the WRAoA than the case of the wing with the fixed wingtip. Although the first structural natural frequency was correctly predicted in the case of the hinged wingtip with torsional spring and overpredicted by 0.1 Hz in the case of the free hinged wingtip, the main natural frequency for the numerical model time response was at a higher frequency with respect to the experimental one. In both cases, the model correctly predicts the fold angle time history and overestimates the damping for the time history response of the WRBM and the vertical displacement of the point considered. The faster decay of the numerical model with respect to the experiments could be due to an overestimation of the load alleviation due to the hinged wingtips.

In the design phase of an aircraft, great importance is given to the maximum WRBM peak because it is the most demanding case. So, the main aim of the aeroelastic models is to capture the WRBM maximum and minimum peaks correctly. Fig. 17 shows the WRBM comparison between the maximum and minimum increment due to the gust measured experimentally and the response calculated by the model considering the three wingtips, a discrete gust with gust lengths from 1.29 m to 4.5 m and the three levels of discrete gust intensity. In the case of the small discrete gust intensity, the model correctly predicts the maximum peaks for all the cases. Increasing the discrete gust intensity, the model underpredicts the maximum peaks. Moreover, Fig. 17 shows the effect of the WRAoA. Indeed for the fixed wingtip, the maximum and minimum peaks are less affected by the WRAoA than the hinged wingtips. In the case of the fixed wingtip,

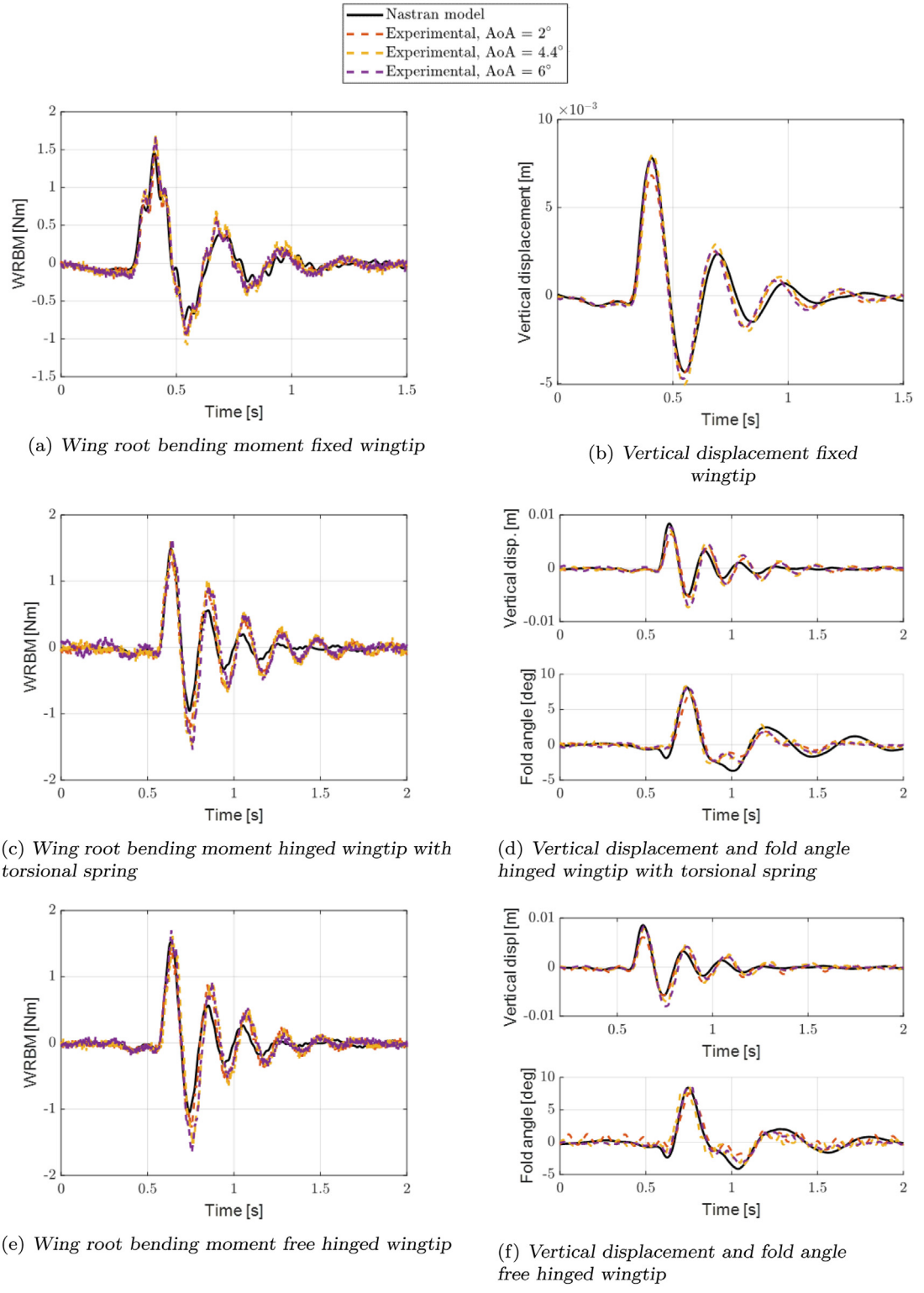

(a) *Wing root bending moment fixed wingtip*

(b) *Vertical displacement fixed wingtip*

(c) *Wing root bending moment hinged wingtip with torsional spring*

(d) *Vertical displacement and fold angle hinged wingtip with torsional spring*

(e) *Wing root bending moment free hinged wingtip*

(f) *Vertical displacement and fold angle free hinged wingtip*

Fig. 16. Comparison between numerical and experimental interesting quantities for the wing with the basic wingtips. Medium intensity discrete gust with gust length of 1.8 m.

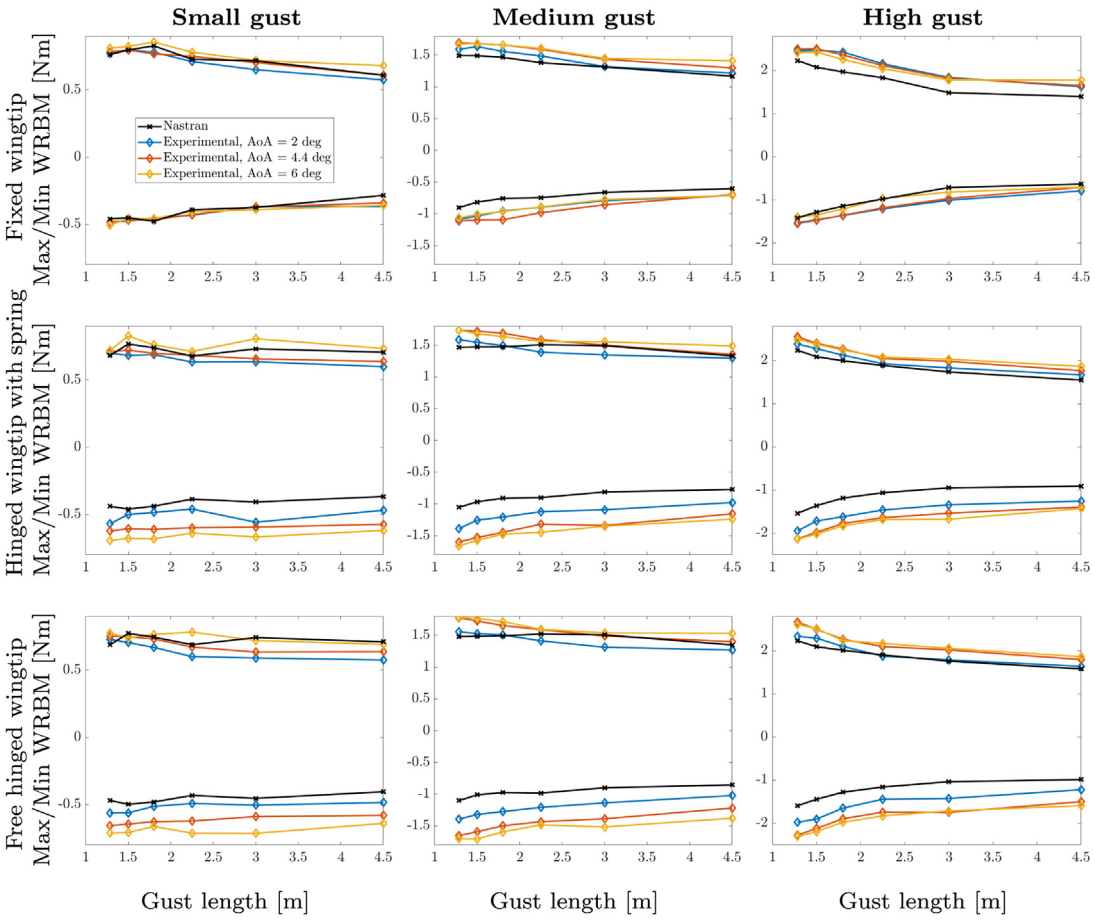

Fig. 17. Wing root bending moment maximum peaks for all the cases considered for the wing with the basic wingtips.

the model correctly predicts the negative peaks; in contrast, in the case of the hinged wingtip, due to the complicated interaction between the flow and the moving wing and wingtip, the negative peaks are consistently underestimated.

7. Investigation of wingtip mass effect

In the previous sections, experimental results suggested that due to the high wingtip mass, the basic hinged wingtip alleviates the gust WRBM for any WRAoA and gust intensity only for gusts with a gust length of 9 m. To analyse the effect of the wingtip mass, simulations were performed considering a modified version of the models developed (light wingtip), and a new hybrid wingtip was tested in the wind tunnel.

7.1. Initial wingtip mass investigation

Two new models were obtained from the wing models with the fixed and free-hinged basic wingtip by reducing the wingtip mass and inertia by 75%. In the rest of this section, they will be called the light–hinged wingtip and the light–fixed wingtip. Simulations at 18 m/s and discrete gusts with gust lengths from 1 m to 10 m and a maximum amplitude of 0.5 m were considered.

Fig. 18 compares the WRBM maximum and minimum peaks for the models with the fixed and free-hinged wingtip in the cases of the basic and light wingtip. The light–hinged wingtip is able to alleviate the maximum WRBM peaks in all the cases, while the negative WRBM peaks are alleviated only when the gust length is greater than 4 m. The attenuation of the maximum WRBM peak is 17% in the case of the basic–hinged wingtip, and 15% in the case of the light–hinged wingtip.

The two free hinged wingtip models are considered to analyse the effects of a lighter wingtip Figs. 19 and 20 show the WRBM and the fold angle, respectively. The lighter wingtip can alleviate the maximum positive and negative WRBM. Reducing the mass of the wingtip allows the wingtip to react more quickly. Indeed for the light wingtip, the fold angle rotates positively as the first effect due to the gust.

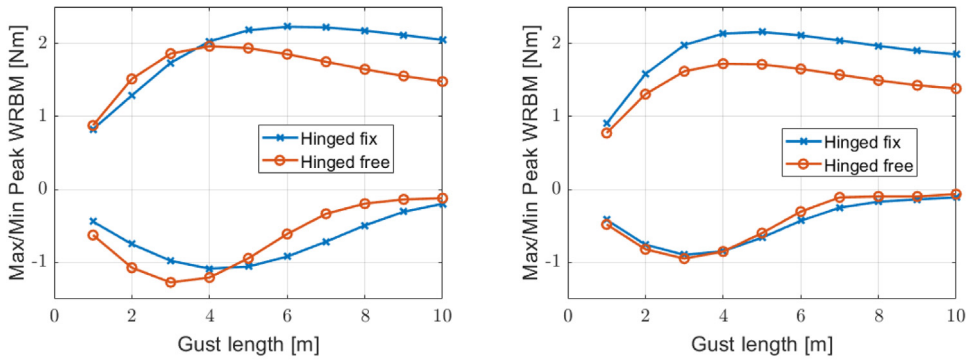

(a) *Basic wingtips* (b) *Light wingtips*

Fig. 18. Wing root bending moment maximum peaks for different wingtips.

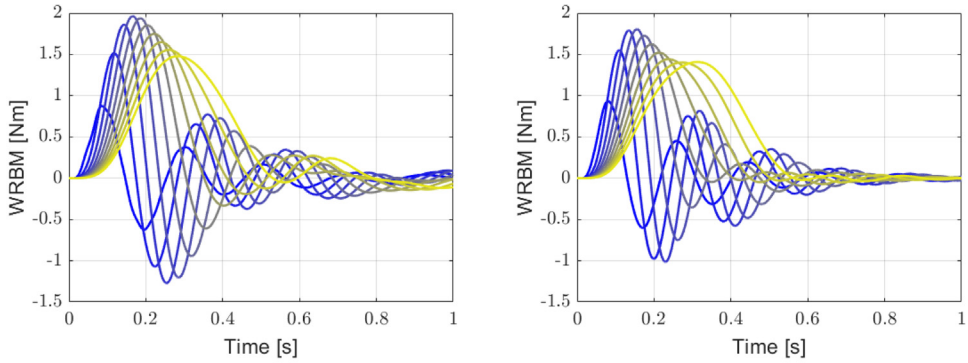

(a) *Basic wingtip* (b) *Light wingtip*

Fig. 19. Wing root bending moment time response for gust lengths of 1 m (blue) to 10 m (yellow). (For interpretation of the references to colour in this figure legend, the reader is referred to the web version of this article.)

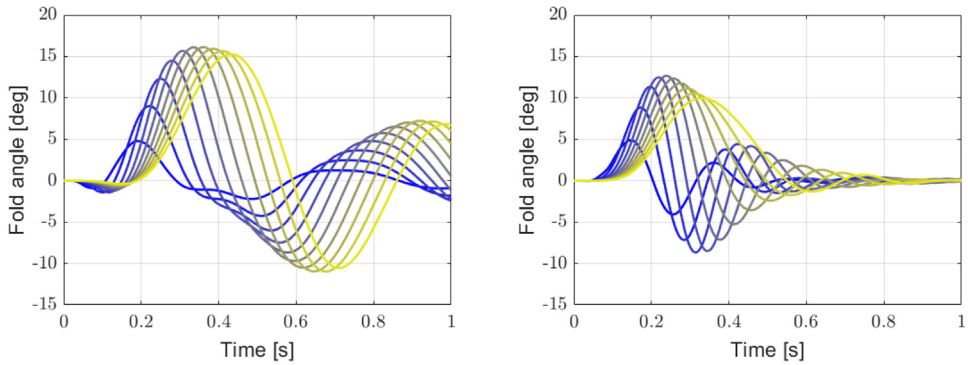

(a) *Basic wingtip* (b) *Light wingtip*

Fig. 20. Fold angle time response for gust lengths 1 m (blue) to 10 m (yellow). (For interpretation of the references to colour in this figure legend, the reader is referred to the web version of this article.)

7.2. Numerical and experimental study of the wingtip centre of mass location

To experimentally verify the effect of a lighter wingtip, a wingtip with the same dimension as the previously discussed wingtip, made of 3D-printed material and high-density insulating foam (called the hybrid wingtip in the rest of this paper), was tested (Balatti et al., 2023). The hybrid wingtip has a free hinge with a flare angle of 10° at 80% of the total wingspan. In the hybrid wingtip, a metal bar able to translate perpendicular to the free stream was added to allow the use of the

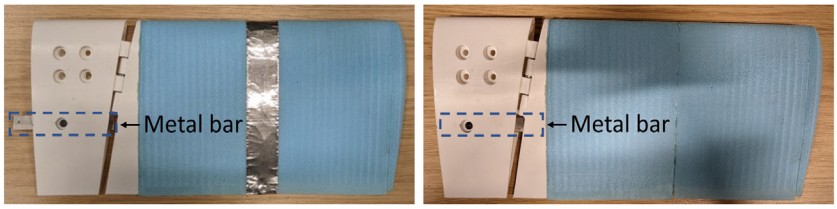

(a) *Hybrid-free hinged wingtip* (b) *Hybrid-fixed wingtip*

Fig. 21. Hybrid wingtip.

Table 6
Mass of the basic, light and hybrid wingtips.

Basic Wingtip		Light wingtip		Hybrid wingtip	
Component	Mass [g]	Component	Mass [g]	Component	Mass [g]
Spar section	40	Spar section	10	Spar section	40
Hinge	3.8	Hinge	3.8	Hinge	3.8
Wingtip assembly	193.8	Wingtip assembly	50.3	Wingtip assembly	77.0
Metal plate	≈0			Metal bar (locking)	21.0

Table 7
Structural natural frequencies below 50 Hz and damping ratios of the wing with the hybrid wingtips measured experimentally and calculated from the models.

Fixed Wingtip				Hinged wingtip
Measured [Hz]	Calculated [Hz]	Error [%]	Damping ratio [%]	Calculated [Hz]
–	–	–	–	4.1
4.4	4.4	0	0.2	5.6
23.6	23.9	1.3	0.6	24.1
27.5	27.0	1.8	0.2	29.1

same wingtip as a free-hinged wingtip as well as a fixed wingtip. Fig. 21 shows the hybrid wingtip. Two threaded holes along the metal bar ensure it does not move when it is in its retracted position, and the hinge is free, as in Fig. 21(a), and in its extended position, and the hinge is fixed, as in Fig. 21(b). Table 6 gives the wingtip mass summary for the basic wingtip and the hybrid wingtip. The mass of the hybrid wingtip is 78% of the basic wingtip.

7.2.1. Experimental measurements

Based on the model of Section 3 two aeroelastic models representative of the wing with the hinged–hinged wingtip and with the hybrid–fixed wingtip were defined. Impact hammer tests of the wing with the hybrid wingtips were performed to extract structural natural frequencies and damping ratios. To perform the test on the wing with the hybrid–hinged wingtip, the wing was hung vertically with the wing root clamped at the top to ensure the wingtip was parallel to the main wing. The impact hammer test was not performed because, due to the low wingtip weight, the friction in the hinge prevented the wingtip from oscillating freely. Table 7 reports the identified natural frequencies and damping ratios of the wing with the hybrid–fixed wingtip.

Experimental gust response tests were performed in the wind tunnel considering the wing with the hybrid–hinged and hybrid–fixed wingtip. Discrete gusts with gust lengths from 1.29 m to 9 m, an airspeed of 18 m/s and WRAoAs of 0°, 1° and 4° were considered. Fig. 22 shows the time history gust response increment from the trim for the WRBM and the estimated fold angle. In all the cases, the positive WRBM increment in the case of the hinged wingtip has a smaller amplitude than the one with the fixed wingtip, while the negative WRBM increment has the opposite trend. Indeed when the gust reaches the wing, the WRBM and the fold angle increase together, generating on the wingtip a local negative WRAoA, which produces a negative bending moment and consequently alleviates the load. After reaching its maximum value, the fold angle becomes negative with a time delay with respect to the WRBM, generating an amplification of the load.

Fig. 23 shows the maximum and minimum WRBM increment from the trim value due to the gust for all the tests considered. In all cases, the free-hinged wingtip alleviates the positive WRBM peak while attenuating the negative WRBM peaks in only a few cases. The maximum relative WRBM alleviation is 32% and is achieved in the case of wing WRAoA 1° and a high-intensity discrete gust of gust length of 1.3 m.

7.2.2. Aeroelastic model wing with hybrid wingtip

The aeroelastic model of the wing with the hybrid wingtips was used to calculate their structural natural frequencies. Table 7 compares the structural natural frequencies measured experimentally and calculated from the aeroelastic models

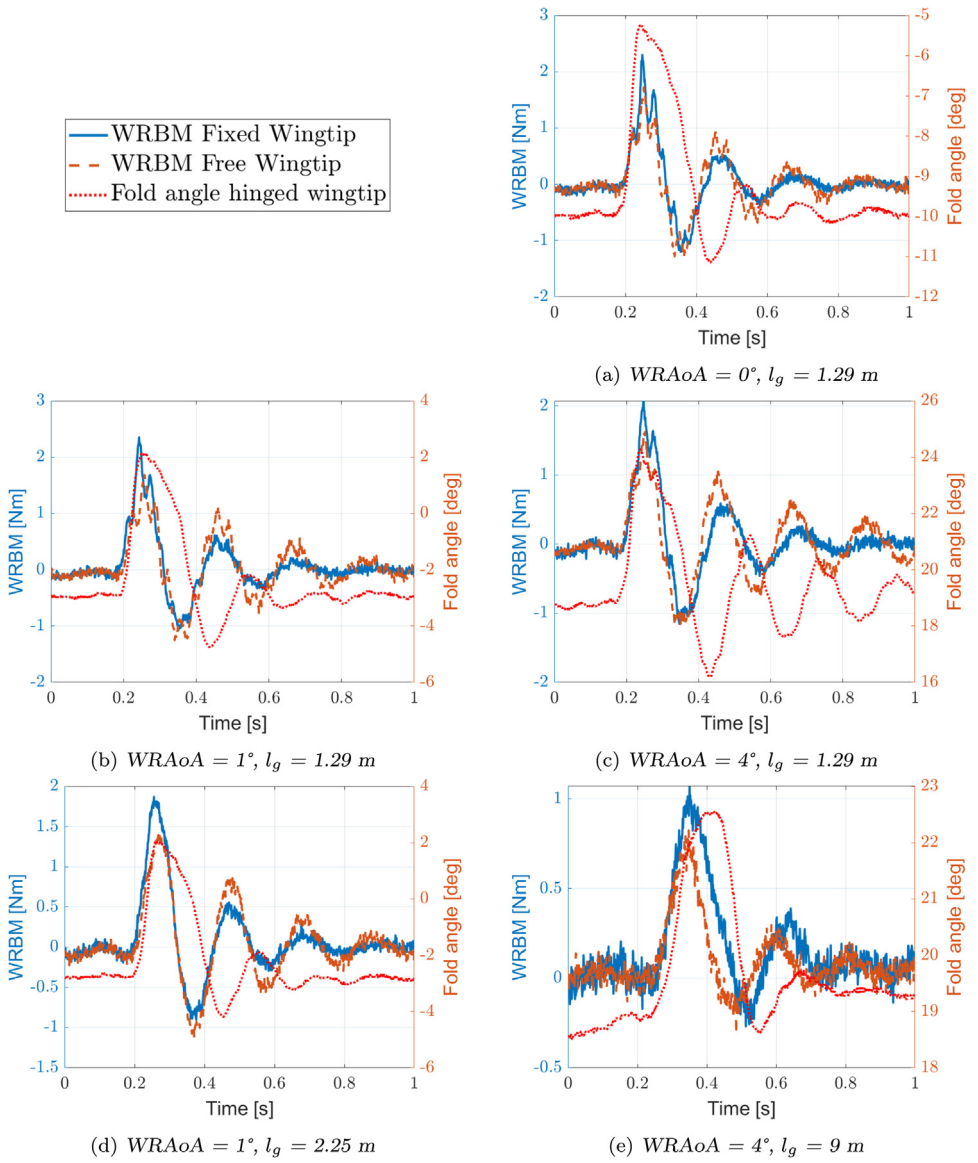

Fig. 22. Wing root bending moment gust response for the wing with the hybrid–fixed and hybrid–hinged wingtip and fold angle time history. Medium discrete gust amplitude at different gust lengths and WRAoAs 0°, 1° and 4°.

and reports the identified structural damping ratios for the wing with the hybrid–fixed wingtip. The structural damping was tailored to match the gust response measurements in the case of the wing with the hybrid–hinged wingtip.

As in the previous analysis, the numerical and experimental results were compared in terms of gust time history responses of the interesting quantities. Fig. 24 shows the comparison between the numerical and experimental gust responses in the case of the hybrid–fixed wingtip, Figs. 24(a) and 24(b), and the hybrid–free hinged wingtip, Figs. 24(c) and 24(d). The experimental measurements of the wing with the hybrid–hinged wingtip are more affected by the WRAoA than the measurements of Fig. 16. The model correctly predicts the WRBM time history when the WRAoA is 0° and 1°, the vertical displacement time history for all the WRAoA, and the fold angle time history in the case of WRAoA 4°.

Fig. 25 compares the maximum and minimum WRBM increment due to the gust measured experimentally and calculated by the model considering the three levels of discrete gust intensity. In the case of the small discrete gust intensity, the model correctly predicts the maximum peaks for all the cases. By increasing the discrete gust intensity, the model underpredicts the peaks.

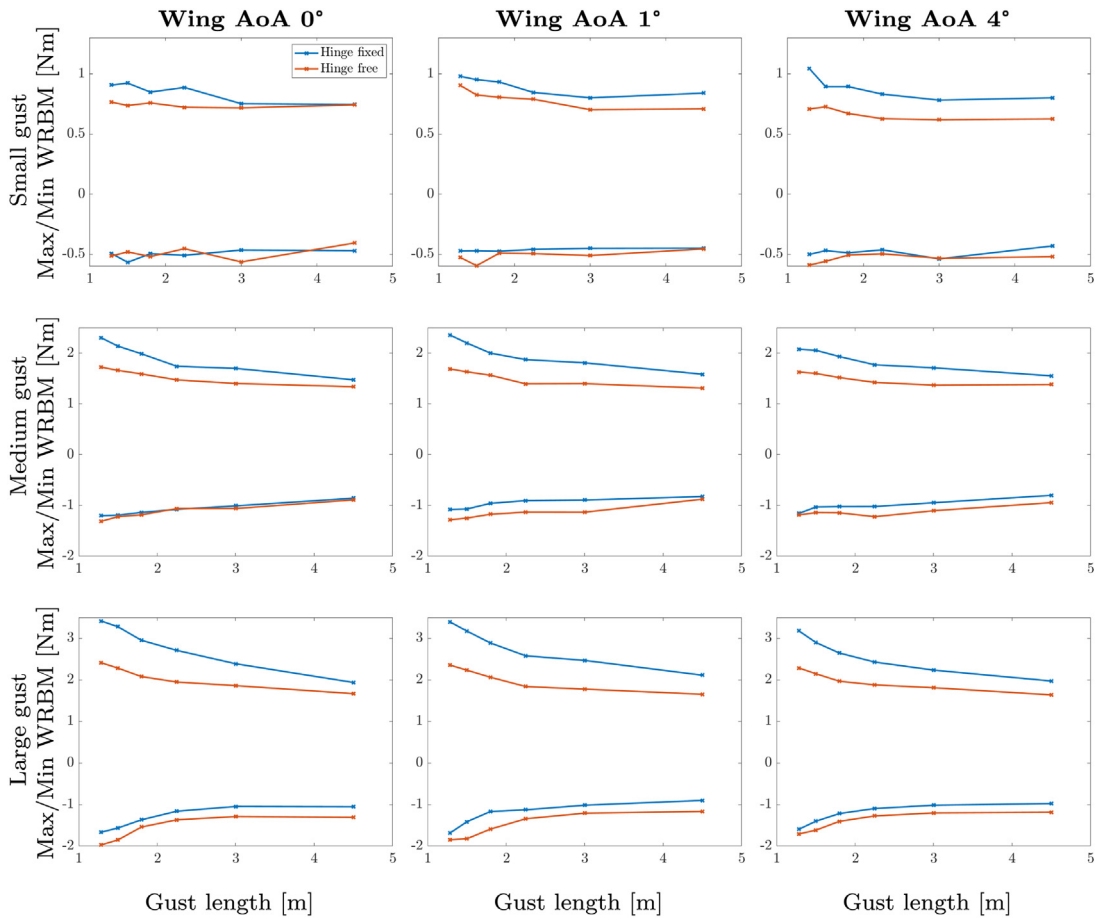

Fig. 23. Wing root bending moment maximum peaks for all the cases considered in the case of the wing with the hybrid wingtip.

7.3. Comparison light and hybrid wingtip

In this section, a comparison between the gust responses from the wing with the hybrid and the light wingtips is performed. The mass of the light wingtips is 37.5 g, similar to the mass of the hybrid wingtip (33.2 g), but it has a different weight distribution and centre of mass location. Simulations at 18 m/s and discrete gusts with gust lengths from 1 m to 10 m and a maximum amplitude of 0.5 m were considered. Fig. 26 compares the maximum and minimum WRBM gust response peaks for the model with the hybrid–fixed and hybrid–hinged wingtip. Figs. 18 and 26 show that both hybrid and light hinged wingtip are able to alleviate the maximum WRBM peaks in all the cases, while the negative WRBM peaks are alleviated only when the gust length is greater than 4 m. Moreover, the hybrid wingtip has better gust load alleviation performance than the light wingtip. The attenuation of the maximum WRBM peak is 19% in the case of the hybrid–hinged wingtip.

Fig. 27 shows the WRBM and the fold angle time response for the hybrid–hinged wingtip. Figs. 18 and 26 show that in the case of the light–hinged wingtip and hybrid–hinged wingtip for very short discrete gusts (e.g. gust lengths equal or smaller than 4 m), the wingtip does not rotate quickly enough to be able to alleviate both positive and negative peaks. Indeed, the positive peak is alleviated because the wingtip is rotating positively when the WRBM reaches its maximum, and its angle is positive when the WRBM reaches its minimum. Figs. 19(b) and 27(a) confirm that the hybrid–hinged wingtip rotates faster than the light–hinged wingtip, achieving better load alleviation for very short discrete gusts. Moreover, the hybrid–hinged wingtip produces a smaller intensity negative WRBM by having a smaller positive fold angle when the WRBM is minimum and alleviating the WRBM first peak and consequently reducing the wingtip inertia moment, with respect to the light–hinged wingtip. Finally, the responses of the light–hinged wingtip are more damped with respect to the hybrid–hinged wingtip.

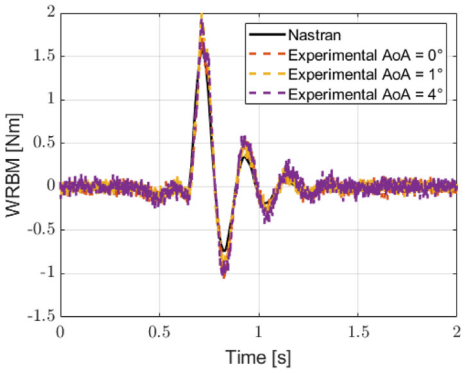

(a) *Wing root bending moment hybrid-fixed wingtip*

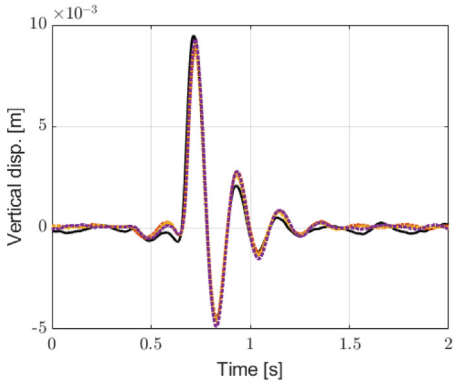

(b) *Vertical displacement hybrid-fixed wingtip*

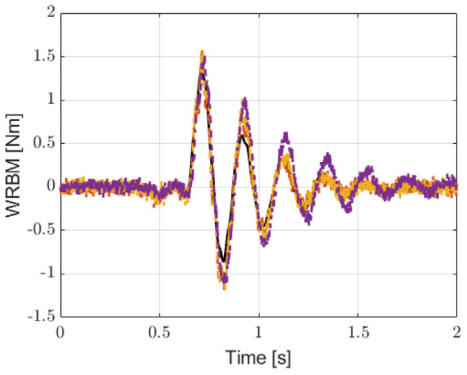

(c) *Wing root bending moment hybrid-hinged wingtip*

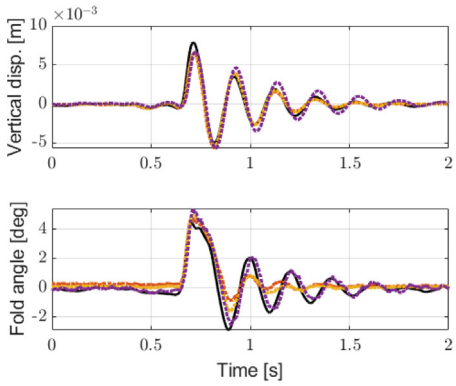

(d) *Vertical displacement and fold angle hybrid-hinged wingtip*

Fig. 24. Comparison between numerical and experimental interesting quantities of the wing with the hybrid wingtips. Medium intensity discrete gust with gust length of 1.8 m.

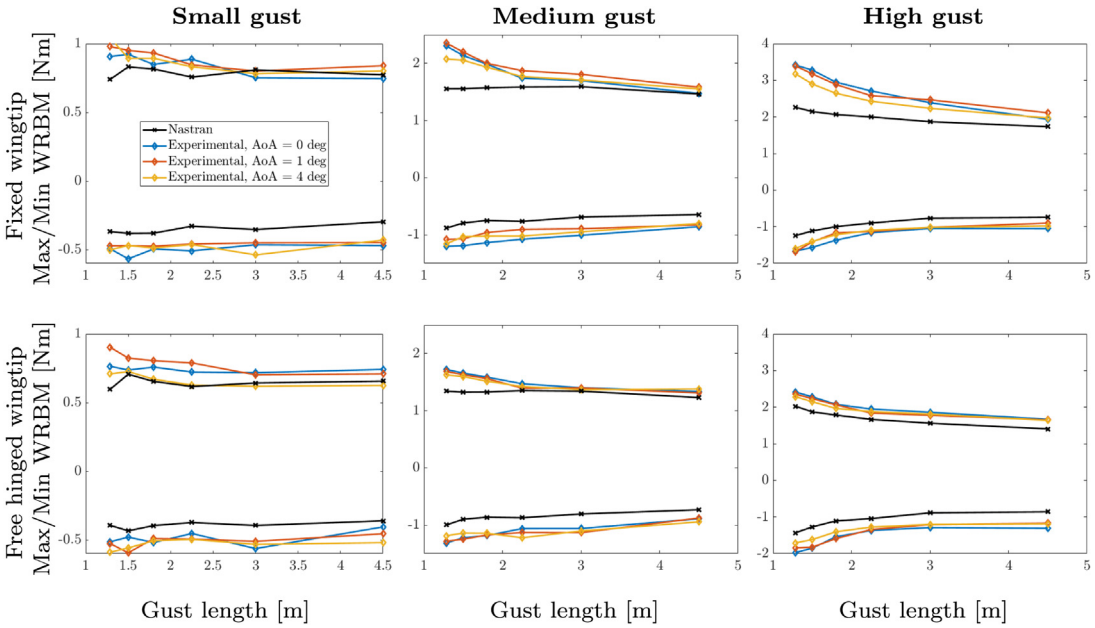

Fig. 25. Wing root bending moment maximum peaks for all the cases considered for the wing with the hybrid wingtips.

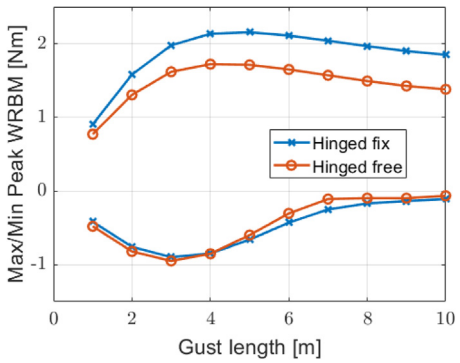

Fig. 26. Wing root bending moment maximum peaks for the hybrid wingtips.

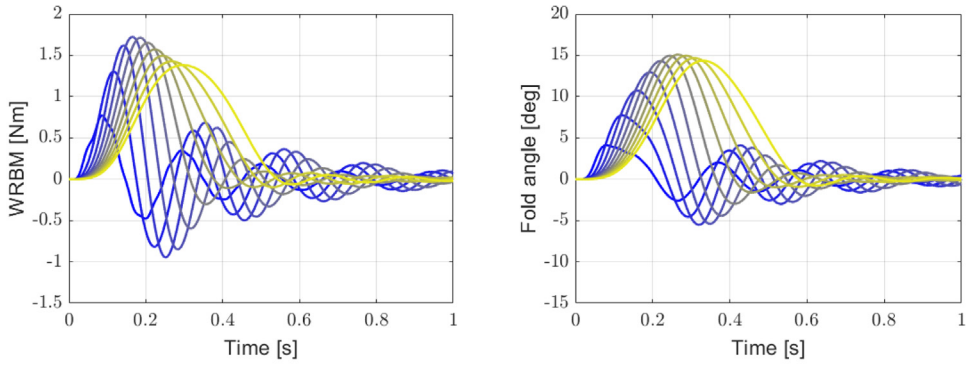

(a) *Wing root bending moment* (b) *Fold angle*

Fig. 27. Time response for gust lengths 1 m (blue) to 10 m (yellow) for the wing with the hybrid hinged wingtip. (For interpretation of the references to colour in this figure legend, the reader is referred to the web version of this article.)

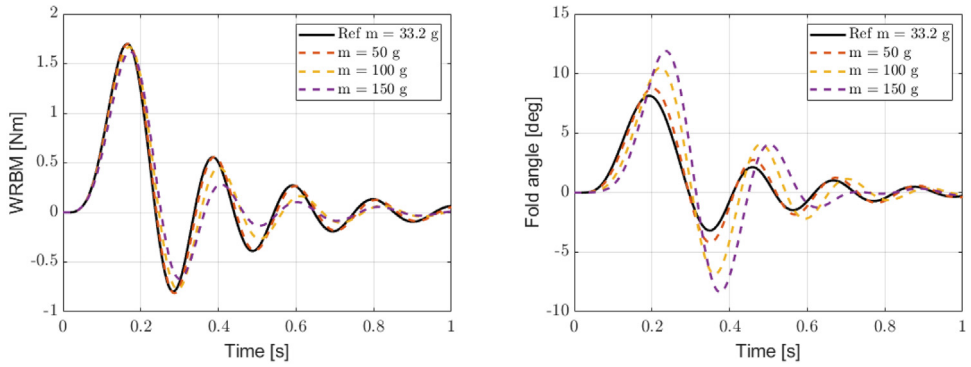

(a) *Wing root bending moment* (b) *Fold angle*

Fig. 28. Gust response for different wingtip masses.

7.4. Wingtip sensitivity analysis

A sensitivity analysis was performed to analyse the effect of the wingtip mass, the longitudinal position of the wingtip centre of mass, and the hinge stiffness. In each analysis, the hybrid–hinged wingtip model was considered as the reference model and one parameter was modified at a time. Figs. 28–30 show the WRBM and fold angle gust response to a discrete gust with a gust length of 4 m. Increasing the wingtip mass decreases the maximum and minimum WRBM peaks and the wingtip natural frequency and increases the maximum and minimum fold angle peaks and the aeroelastic damping. Despite increasing the wingtip mass, the first positive WRBM peak occurs for a lower fold angle, and the first negative WRBM peak occurs for a higher positive fold angle. Increasing the wingtip mass, the positive and minimum WRBM peaks

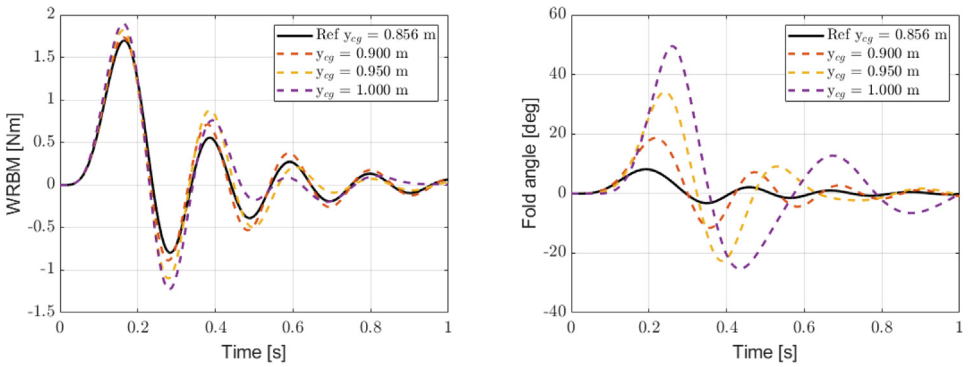

(a) *Wing root bending moment* (b) *Fold angle*

Fig. 29. Gust response for different longitudinal locations of the wingtip centres of mass.

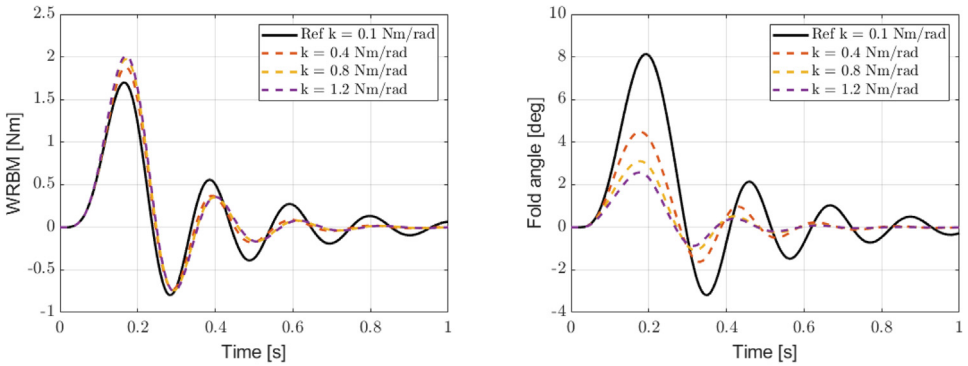

(a) *Wing root bending moment* (b) *Fold angle*

Fig. 30. Gust response for different hinge wingtip stiffnesses.

decrease. Indeed, increasing the wingtip mass decreases its natural frequency and reduced frequency, increasing both the unsteady aerodynamic lift produced by the wingtip and its load alleviation.

Increasing the spanwise distance of the wingtip centre of mass from the hinge increases the wingtip structural inertia, which creates higher fold angle oscillations and lowers the structural natural frequencies. Although the wingtip oscillation has higher intensity, increasing the spanwise distance of the wingtip centre of mass from the hinge of the wingtip centre of mass increases the delay between the gust and the fold angle rotation, causing a lower fold angle when the WRBM reaches its maximum and a large positive angle when the WRBM reaches its minimum.

Increasing the wingtip hinge stiffness produces a lower fold angle amplitude, limiting the alleviation of the first WRBM peak. Moreover, it improves the synchronisation between the WRBM and the fold angle and, consequently, the load alleviation capability of the first negative peak. Increasing the wingtip hinge stiffness increases the natural frequency of the first structural out-of-plane bending mode and its aeroelastic damping.

8. Conclusion

A wing able to accommodate different wingtips, i.e. a fixed wingtip, a free hinged wingtip and a hinged wingtip with a torsional spring, was manufactured and tested in the Swansea University wind tunnel. Structural characterisation was performed on the 3D-printed sections, the wing spar and the wing with the manufactured wingtips. Static wind tunnel tests were performed at 10 m/s, 14 m/s, 18 m/s and 22 m/s and they demonstrated the ability of hinged wingtips to reduce gust loads compared to a similar wing with a fixed wingtip. Gust loads measured at the wing root have confirmed that the gust increment due to gusts is smaller for a wing with a hinged wingtip with respect to the fixed wingtip.

Aeroelastic models of the wing with the manufacturing wingtips were developed in Nastran. The comparison between the structural natural frequencies measured experimentally and calculated from the aeroelastic models showed a good agreement. The experimentally measured structural damping and gust time history produced by the gust generator were used to calculate the gust response. The comparison between numerical and experimental gust responses were used to validate the aeroelastic models. The results of the gust response are less accurate for the wing with a hinged wingtip with

respect to the one with a fixed wingtip due to the nonlinearity introduced by the hinge. Moreover, the gust response of the aeroelastic models did not consider the effect due to the WRAoA. In the case of the wing with the fixed wingtip, the experimental results showed that the wing response is slightly affected by the WRAoA. On the contrary, in the case of the hinged wingtip, the results are more affected by the WRAoA. The aeroelastic model correctly predicted the maximum peaks.

The experimental gust response measurements showed the limitation of the 3D-printed wingtip in alleviating gust loads. The validated numerical models demonstrated that by reducing the mass and inertia of the heavy wingtip by 75% (light wingtip), the hinged wingtip reacts faster to gusts and offers improved gust load alleviation performance. Moreover, numerical and experimental results showed that light wingtips react fast, reducing the main WRBM peak while amplifying the first negative WRBM peak. The sensitivity analysis showed that reducing the wingtip mass and structural inertia, or increasing the wingtip mass alone or moving the longitudinal wingtip centre of mass closer to the hinge, improves the load alleviation capability of a hinged wingtip. Furthermore, increasing the hinge stiffness is beneficial only to attenuate the first negative WRBM peak. The wingtips were experimentally tested, and the sensitivity analysis results identified the effects of different wingtip parameters on the gust load alleviation performance of wings with hinged wingtips.

CRediT authorship contribution statement

Davide Balatti: Conceptualization, Methodology, Software, Validation, Formal analysis, Investigation, Data curation, Writing – original draft, Writing – review & editing, Visualization, Project administration. **Hamed Haddad Khodaparast:** Conceptualization, Methodology, Validation, Investigation, Writing – original draft, Writing – review & editing, Visualization, Supervision, Project administration, Funding acquisition. **Michael I. Friswell:** Conceptualization, Methodology, Validation, Investigation, Writing – original draft, Writing – review & editing, Visualization, Supervision, Project administration, Funding acquisition. **Marinos Manolesos:** Investigation, Writing – original draft, Writing – review & editing, Supervision. **Andrea Castrichini:** Investigation, Writing – original draft, Writing – review & editing, Supervision.

Declaration of competing interest

The authors declare that they have no known competing financial interests or personal relationships that could have appeared to influence the work reported in this paper.

Data availability

Data will be made available on request.

Acknowledgements

The research leading to these results has received funding from the Engineering Physical Science Research Council (EPSRC), United Kingdom through a program grant EP/R006768/1. Davide Balatti also acknowledges the PhD scholarship funded by the Faculty of Science and Engineering at Swansea University, United Kingdom.

References

Ajaj, R.M., 2021. Flight dynamics of transport aircraft equipped with flared-hinge folding wingtips. J. Aircr. 58 (1), 98–110.
Allen, J.B., 1999. Articulating winglets. Google Patents. US Patent 5, 988, 563.
Anon, 1951. Knee-action wings cushion ride in french plane. Pop. Sci. Mag. 158, 150.
Balatti, D., Ellis, J.D., JiffrI, S., Haddad Khodaparast, H., Friswell, M.I., 2023. Active hinged wingtip for gust load alleviation and manoeuvres. In: AIAA SCITECH 2023 Forum. p. 2567.
Balatti, D., Haddad Khodaparast, H., Friswell, M.I., Manolesos, M., 2022a. Improving wind tunnel "1-cos" gust profiles. J. Aircr. 59 (6), 1514–1528. http://dx.doi.org/10.2514/1.C036772.
Balatti, D., Khodaparast, H.H., Friswell, M.I., Manolesos, M., 2022b. Aeroelastic model validation through wind tunnel testing of a wing with hinged wingtip. In: International Forum on Aeroelasticity and Structural Dynamics, Madrid, Spain.
Balatti, D., Khodaparast, H.H., Friswell, M.I., Manolesos, M., Amoozgar, M., 2021a. The effect of folding wingtips on the worst-case gust loads of a simplified aircraft model. Proc. Inst. Mech. Eng. G 09544100211010915. http://dx.doi.org/10.1177/09544100211010915.
Balatti, D., Khodaparast, H.H., Friswell, M.I., Manolesos, M., Castrichini, A., 2021b. Aircraft turbulence and gust identification using simulated in-flight data. Aerosp. Sci. Technol. 115, 106805.
Barbarino, S., Bilgen, O., Ajaj, R.M., Friswell, M.I., Inman, D.J., 2011. A review of morphing aircraft. J. Intell. Mater. Syst. Struct. 22 (9), 823–877.
Carrillo, X., Mertens, C., Sciacchitano, A., van Oudheusden, B., De Breuker, R., Sodja, J., 2022. Wing stiffness and hinge release threshold effects on folding wingtip gust load alleviation. In: AIAA SCITECH 2022 Forum. p. 1559.
Castrichini, A., 2017. Parametric Assessment of a Folding Wing-Tip Device for Aircraft Loads Alleviation (Ph.D. thesis). University of Bristol.
Castrichini, A., Cooper, J.E., Wilson, T., Carrella, A., Lemmens, Y., 2017a. Nonlinear negative stiffness wingtip spring device for gust loads alleviation. J. Aircr. 54 (2), 627–641.
Castrichini, A., H Siddaramaiah, V., Calderon, D.E., Cooper, J.E., Wilson, T., Lemmens, Y., 2016. Nonlinear folding wing tips for gust loads alleviation. J. Aircr. 53 (5), 1391–1399.
Castrichini, A., Siddaramaiah, V.H., Calderon, D.E., Cooper, J.E., Wilson, T., Lemmens, Y., 2017b. Preliminary investigation of use of flexible folding wing tips for static and dynamic load alleviation. Aeronaut. J. 121 (1235), 73–94.

Castrichini, A., Wilson, T., Azabal, A., 2018a. Apparatus, aircraft comprising an apparatus and method of performing a descent in an aircraft. Google Patents. Patent App. GB1806556.5A.
Castrichini, A., Wilson, T., Cooper, J., 2018b. On the dynamic release of the semi aeroelastic wing-tip hinge device. In: 6th Aircraft Structural Design Conference.
Castrichini, A., Wilson, T., Saltari, F., Mastroddi, F., Viceconti, N., Cooper, J.E., 2020. Aeroelastics flight dynamics coupling effects of the semi-aeroelastic hinge device. J. Aircr. 57 (2), 333–341.
Cheung, R.C., Rezgui, D., Cooper, J.E., Wilson, T., 2018. Testing of a hinged wingtip device for gust loads alleviation. J. Aircr. 55 (5), 2050–2067.
Cheung, R.C., Rezgui, D., Cooper, J.E., Wilson, T., 2020. Testing of folding wingtip for gust load alleviation of flexible high-aspect-ratio wing. J. Aircr. 57 (5), 876–888.
Conti, C., Saltari, F., Mastroddi, F., Wilson, T., Castrichini, A., 2021. Quasi-steady aeroelastic analysis of the semi-aeroelastic hinge including geometric nonlinearities. J. Aircr. 1–11.
European Aviation Safety Agency, 2020. Certification specifications and acceptable means of compliance for large aeroplanes CS25. https://www.easa.europa.eu/sites/default/files/dfu/CS-25%20Amendment%2024.pdf. (Last Accessed 08 November 2021).
Healy, F., Pontillo, A., Rezgui, D., Cooper, J.E., Kirk, J., Wilson, T., Castrichini, A., 2022. Experimental analysis of the dynamics of flared folding wingtips via a novel tethered flight test. In: AIAA SCITECH 2022 Forum. p. 1757.
Pattinson, J., Wilson, T., Herring, M., 2015. High fidelity simulation of the folding wing tip for loads alleviaton. In: International Forum on Aeroelasticity and Structural Dynamics. IFASD 2015.
Pitt, D., 2004. Static and dynamic aeroelastic analysis of structural wing fold hinges that are employed as an aeroelastic tailoring tool. In: 45th AIAA/ASME/ASCE/AHS/ASC Structures, Structural Dynamics & Materials Conference. p. 1754.
Sanghi, D., Cesnik, C.E., Riso, C., 2023. Roll maneuvers of very flexible aircraft with flared folding wingtips. In: AIAA SCITECH 2023 Forum. p. 0186.
Wilson, T., Castrichini, A., Azabal, A., 2019a. Apparatus, aircraft and method of moving a movably mounted wing tip device. Google Patents. Patent US 16/386, 675.
Wilson, T., Castrichini, A., Azabal, A., Cooper, J., Ajaj, R., Herring, M., 2017. Aeroelastic behaviour of hinged wing tips. In: International Forum on Aeroelasticity and Structural Dynamics. IFASD 2017, Royal Aeronautical Society.
Wilson, T., Herring, M., Pattinson, J., Cooper, J., Castrichini, A., Ajaj, R., Dhoru, H., 2021. An aircraft wing with a moveable wing tip device for load alleviation. Google Patents. Patent US 16/067, 221.
Wilson, T., Kirk, J., Hobday, J., Castrichini, A., 2019b. Small scale flying demonstration of semi aeroelastic hinged wing tips. In: International Forum on Aeroelasticity and Structural Dynamics. IFASD 2019.